1 **Characteristics of Robust Mesoscale Eddies in the Gulf of Mexico**

3 Yingli Zhu, Xinfeng Liang

4 School of Marine Science and Policy, University of Delaware, Lewes, 19958, US

7 *Corresponding to*: Yingli Zhu (yzhu@udel.edu)

10   **Abstract**. Although numerous studies on mesoscale eddies in the Gulf of Mexico (GoM)

11   have been conducted, a comprehensive study on their temporal and spatial characteristics is

12   still lacking. In this study, we combine three eddy detection algorithms to detect eddies from

13   the 26-year sea surface height record in the GoM and examine their characteristics. We find

14   distinct characteristics between Loop Current Eddies (LCEs), Loop Current Frontal Eddies

15   (LCFEs), and mesoscale eddies that are not directly related to the Loop Current (LC).

16   Seasonal variability appears in both the LCFEs and non-LCFE cyclonic eddies and shows

17   large uncertainties. More specifically, more LCFEs are formed in January to July than in

18   August to December, likely related to the seasonal variation of the northward penetration of

19   the LC. And the formation of non-LCFE cyclonic eddies shows a biannual variability, which

20   could be linked to the position and strength of the background current in the western GoM.

21   Low-frequency (interannual to multidecadal) variability is also detected. In the eastern GoM,

22   the extent of northward penetration of the LC can affect the generation of LCFEs and result

23   in low-frequency variations. In the western GoM, the low-frequency variability of eddy

24   occurrence and amplitude could be related to the surface circulation strength. This study can

25   serve as an up-to-date reference for eddy-related investigations in the GoM.

1 Introduction

28   Mesoscale eddies are ubiquitous in the Gulf of Mexico (GoM). Different types of eddies have

29   been identified, such as anticyclonic Loop Current Eddies (LCEs), cyclonic Loop Current

30   Frontal Eddies (LCFEs), and eddies that are not directly related to the Loop Current (LC).

31   Those eddies are crucial in transporting heat, salt/freshwater, and other materials and affecting

32   the bottom currents in the GoM (e.g., Beron-Vera et al., 2018; Brokaw et al., 2019; Chang &

33   Oey, 2010; Meunier et al., 2018; Zhu & Liang, 2020). Besides, those eddies can modify the

34   atmospheric environment. In particular, hurricanes in the GoM can be intensified when

35   encountering warm-core rings by absorbing a large amount of heat from eddies (e.g., Bosart et

36   al., 2000; Hong et al., 2000).

37   Various measurements, including drifters, gliders, mooring, and satellite data, have been used

38   to characterize eddies in the GoM (e.g., Elliott, 1982; Hamilton, 1992; Hamilton, 2007;

39   Hamilton et al., 1999; Kirwan et al., 1984; Lewis et al., 1989; Meunier et al., 2018;

40   Paluszkiewicz et al., 1983; Rivas et al., 2008; Rudnick et al., 2015; Vukovich & Maul, 1985;

41   Zhang Y. et al., 2019). Some eddy characteristics, such as diameter and propagation speed,

42   have been reported in previous studies. In the eastern GoM where the LC is the dominant

43   circulation feature, LCEs with a warm and salty core are shed irregularly from the LC through

44   dynamic instability (e.g., Hurlburt & Thompson, 1980; Pichevin & Nof, 1997; Sturges &

45   Leben, 2000; Yang et al., 2020). The shedding time of LCEs has been shown to be related to

46   the seasonal winds in the GoM and the Caribbean Sea (CS) (Chang & Oey, 2012) and

47   fluctuations from the CS (Chang & Oey, 2012, 2013; Murphy et al., 1999; Oey et al., 2003).

48   LCEs have a diameter of 200 to 400 km, a surface swirling speed exceeding 0.5 m s^{-1}, and an

49   average propagating speed of 2 to 5 km day^{-1} (e.g., Elliott, 1982; Kirwan et al., 1984; Kirwan

50   et al., 1988; Vukovich & Crissman, 1986). After separating from the LC, LCEs bring warm

51   and high-salinity water originating from the CS to the western GoM, and the LCE path occupies

52   a broad band in the center of the basin with a mean west-southwest track (Hamilton et al.,

53   1999). When LCEs travel to the western GoM and encounter the western boundary, companion

54   cyclones can be generated (Frolov et al., 2004; Smith, 1986; Vidal et al., 1992). Besides the

55   eddy-topography interaction, LCEs can be cleaved into two parts by interacting with deep

56   water cyclones (Biggs et al., 1996).

57   In addition to LCEs, mesoscale cyclonic eddies (CEs) with relatively small diameters of 80 to

58   150 km have also been detected in the GoM (Hamilton, 1992; Jouanno et al., 2016; Le Hénaff

59   et al., 2014; Vukovich & Maul, 1985; Vukovich, 2007). The commonly seen CEs in the eastern

60   GoM are cold-core LCFEs that are formed on the LC's periphery as a result of the barotropic

61   and baroclinic instabilities (e.g., Chérubin et al., 2006; Donohue et al., 2016a; Fratantoni et al.,

62   1998; Jouanno et al., 2016; Maslo et al., 2020; Vukovich & Maul, 1985; Yang et al., 2020;

63   Zavala-Hidalgo et al., 2003). The topographic vortex stretching can play a role in the

64   intensification of LCFEs (Le Hénaff et al., 2012; Le Hénaff et al., 2014). Also, eddies with a

65   median radius of 30 km have been observed on the northern GoM slope from drifter orbits and

66   hydrographic surveys (e.g., Hamilton, 2007). The small-scale slope eddy activity was

67   speculated to be related to the LC extension and LCE detachment. Some eddies on the northern

68   GoM slope that are not likely related to the LC have also been observed (Hamilton, 1992;

69   Hamilton et al., 2002). Besides, Caribbean eddies can squeeze into the GoM through the

70   Yucatan Channel (Huang et al., 2013; Huang et al., 2021; Murphy et al., 1999), but the eddy

71   number is relatively small.

72   Statistical and comprehensive analyses of eddies over the whole GoM using in situ data and

73   satellite infrared or ocean color data are difficult (e.g., Vukovich, 2007). In situ data cannot

74   give continuous monitoring over the whole GoM. The nearly uniform sea surface temperature

75   (SST) in summer and the extensive cloud cover hinder us from discerning eddies from the

76   satellite infrared or ocean color maps (e.g., Sturges & Leben, 2000; Vukovich & Maul, 1985).

77   In contrast, altimeter observed sea surface height (SSH) data are available in all weather

78   conditions and are the most complete source of detecting mesoscale eddies. Although some

79   temporal and spatial distributions of eddy characteristics have been obtained from the absolute

80   dynamic topography (ADT) maps or along-track SSH anomalies, they are based on short-

81   period altimeter data with record lengths of 2 to 4 years (Brokaw et al., 2020; Leben & Born,

82   1993) or are focused on one specific type of eddy, such as the LCE (e.g., Leben, 2005; Hall

83   and Leben, 2016) or LCFE (Le Hénaff et al., 2014). For example, by tracking SSH contour (17

84   cm) and its breaking from the LC in the GoM, LCE separations have been determined over the

85   first 12-year (Leben, 2005) and 20-year altimetry period (Hall and Leben, 2016). A significant

86   peak in the timing of LCE separation in August and September and a less significant peak in

87   February and March have been observed (Hall & Leben, 2016; Vukovich, 2012). An increasing

88   number of LCEs in the decade 2001-2010 was also found (Lindo-Atichati et al., 2013;

89   Vukovich, 2012).

90   The seasonal and interannual variabilities of mesoscale eddies are important and closely related

91   to that of the large-scale circulation, from which eddies obtain energy (e.g., Yang et al., 2020).

92   As the dominant circulation system in the eastern GoM, the LC has been shown to be more

93   intrusive from January to July on the seasonal time scale (Hamilton et al., 2014) and from 2002

94   to 2006 than in 1993 on the interannual time scale (Alvera-Azcárate et al., 2009). The climate

95   variability in the GoM has been related to remote climate forcing such as El Niño-Southern

96   Oscillation (ENSO) and North Atlantic Oscillation (NAO) (e.g., Rodriguez-Vera et al., 2019).

97   Therefore, the eddy activity in the GoM could be affected by various climate modes, such as

98   ENSO (e.g., Philander, 1990), NAO (e.g., Wallace & Gutzler, 1981), and Atlantic Meridional

99   Mode (AMM) (e.g., Chiang & Vimont, 2004). However, characteristics of different types of

100 eddies in the GoM, such as propagation, seasonal, and low-frequency (interannual to

101 multidecadal) variability, are not clear and need more examination. Nowadays, with the

102 satellite observed SSH data that span more than 26 years, we can conduct a more

103 comprehensive analysis of the characteristics of mesoscale eddies in the GoM.

104 To detect and describe eddies, a variety of automatic eddy detection and tracking algorithms

105 have been developed. Chelton et al. (2007) used the physical Okubo-Weiss (OW) parameter

106 (Okubo, 1970; Weiss, 1991) to detect mesoscale eddies. Geometric properties, such as the

107 closed SSH or streamline contours, have also been used to define eddy domains (e.g.,

108   Chaigneau et al., 2008; Chelton et al., 2011; Faghmous et al., 2015; Le Vu et al., 2018).

109   Moreover, hybrid methods that combine the physical parameters and geometric properties have

110   been proposed to discern mesoscale eddies (Halo et al., 2014; Kang & Curchitser, 2013). The

111   17-cm SSH contour has also been widely used to define the LC front, and separation events of

112   LCE are identified by breaking of the 17-cm tracking contour with no later reattachment

113   (Leben, 2005; Hall and Leben, 2016). Different eddy detection algorithms have their

114   advantages and drawbacks. For example, the OW method is sensitive to the noise in the SSH

115   data, and the approaches that use geometrical properties are sensitive to the interval searching

116   for closed contours (Le Vu et al., 2018; Lian et al., 2019). There is no best algorithm because

117   the eddy definition is elastic among different studies (Kurian et al., 2011).

118   In this study, to find eddies that are less sensitive to the eddy detection algorithms, a method

119   that combines three previously used eddy detection algorithms is developed and applied to the

120   26-year SSH maps in the GoM. Characteristics of robust eddies in the GoM are derived by

121   examining the eddies detected with the new method. The paper is organized as follows: data

122   and details of the eddy detection and tracking algorithms are presented in Sect. 2.

123   Characteristics of the detected eddies, including eddy trajectories, basic eddy characteristics,

124   seasonal and low-frequency variabilities of eddies are reported in Sect. 4. Conclusions and

125   discussions are given in Sect. 5.

126   **2 Data and Methods**

127   **2.1 Data**

128   Delayed time 2018 (DT2018) gridded ADT data (Taburet et al., 2019) from two altimeter

129   satellites (twosat product) provided by the Copernicus Climate Change Service (C3S) were

130   used for eddy detection and the subsequent examination of eddy characteristics. DT2018

131   gridded ADT data from multiple satellites (allsat product) provided by the Copernicus Marine

132   Environment Monitoring Service (CMEMS) were also used for the discussion of the influence

133   of satellite sampling on eddy detection. The ADT data span from 1 January 1993 to 13 May

134   2019 with a daily time interval. ADT data rather than sea level anomalies (SLAs) were selected

135   because artificial eddies could be identified in SLAs (e.g., Laxenaire et al., 2018; Pegliasco et

136   al., 2021). Note that although the spatial resolution of the ADT provided is 0.25 degrees, its

137   effective spatial resolution is controlled by many factors, such as the along-track smoothing

138   and the spatial correlation scale (Pujol et al., 2016).

139   To examine the effective spatial resolution of the gridded ADT product in the GoM,
140   TOPEX/Poseidon (T/P) along-track ADT data from 2 January 1996 to 3 December 1999 were
141   compared with the twosat gridded ADT data (Fig. 1). Gridded ADT data were first linearly
142   interpolated to the ground tracks shown in Fig 1a. The wavenumber spectra of the along-track
143   and interpolated ADT data along one sample T/P track were then calculated and averaged over
144   the selected T/P period (Fig. 1b). Compared to the along-track ADT, the spectrum of the
145   gridded ADT decreases by 50% at the wavelength of 200 km, which represents the effective
146   spatial resolution of the gridded ADT data in the GoM. This finding is consistent with the
147   spatial correlation scales used in the gridded product processing (Pujol et al., 2016) and
148   corresponds to an e-folding scale of about 37 km for an individual eddy (Chelton et al., 2011).
149   The interpretation of filter cutoff wavelength in terms of the corresponding eddy scale is based
150   on eddy shape that is approximated as an axially symmetric Gaussian structures (Chelton et al.,
151   2011). Chelton et al. (2011) showed that a half-power point at a wavelength of 2° corresponds
152   to a Gaussian feature in space with an e-folding scale of 0.37°. Therefore, the gridded ADT
153   product in the GoM can only resolve eddies with a radius larger than 37 km, and eddies with a
154   radius smaller than 37 km are not considered in this study. The gridded products cannot capture
155   the small-scale eddies (Amores et al., 2018). It should be noted that eddies that lie in the
156   "diamond-shaped" area between the satellite tracks cannot be fully resolved. The eddy
157   amplitude could be underestimated due to the smoothing during the data generation process.
158   We focus on the spatial and temporal variability when we examine the eddy amplitude.
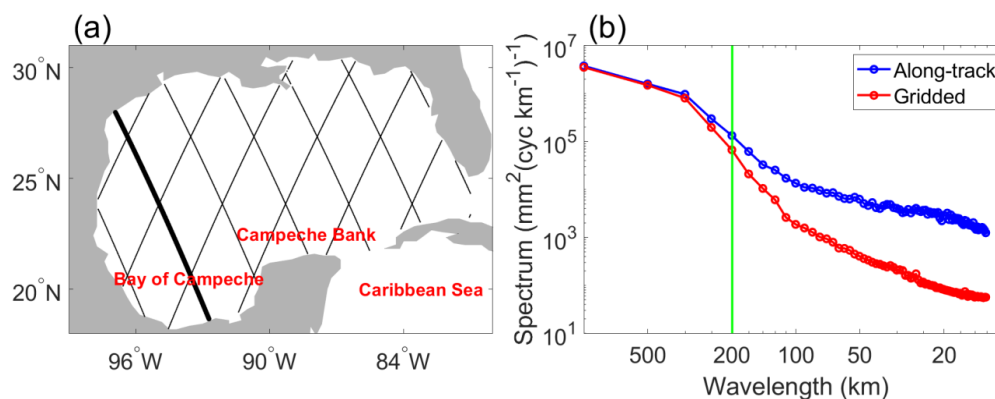
159

160   **Figure 1**: (a) Ground tracks of the TOPEX/Poseidon satellite in the GoM. The thick black line
161   represents the track along which the wavenumber spectrum of ADT was estimated. (b)
162   Wavenumber spectrum of along-track and gridded ADT along the track marked by the thick
163   black line in (a). The vertical green line marks the wavelength of 200 km.

164

165   ADT data were further processed before they were used to detect eddies. First, since altimetry

166   observations near the coast are less reliable (Castelao & He, 2013; Saraceno et al., 2008), ADT

167   data at grid points that are 30 km or less away from the coast were discarded. Second, to make

168   eddy features stand out from the large-scale background SSH field, a two-dimensional spatial

169   filter with a cut-off wavelength of 1000 km was applied to the gridded ADT data. The spatial

170   filtering removes the large-scale variability of SSH that is dominated by the seasonal steric

171   height, which is similar to removing the daily spatial average ADT over the deep-water GoM.

172   Third, because the LC has a shape of a loop, which is different from isolated mesoscale eddies

173   but might be recognized as eddy by the eddy detection algorithms, the LC was isolated so that

174   no eddy was considered within the LC. Leben (2005) used the 17-cm contour of ADT to define

175   the LC front. As the mean reference SSH field in this study was different from that used in

176   Leben (2005), we used the 25-cm contour of the SSH anomalies to define the LC front. Because

177   we would like to eliminate the spatially uniform variability of SSH in the GoM, the SSH

178   anomalies with the spatially mean SSH removed were used to find the LC front. The northern

179   boundary of the LC obtained using the 25-cm contour of SSH anomalies shows similar

180   variability as that reported in Leben (2005). Eddy detection and tracking algorithms were then

181   applied to the high-passed ADT fields.

182   Other variables were also explored to explain some of the detected eddy characteristics. The

183   global atlas of the first-mode Rossby radius of deformation (Chelton et al., 1998) was used to

184   calculate the standard first-mode Rossby wave propagation velocity, $c = -\beta R^2$, where β is the

185   meridional variation of the Coriolis parameter and R is the first-mode Rossby radius of

186   deformation. Moreover, the multivariate ENSO index (MEI V2) (Zhang T. et al., 2019), NAO

187   index (Hurrell, 1995), and AMM index (Chiang & Vimont, 2004) were used to examine

188   possible relationships between the eddy activity in the GoM and climate modes.

189   2.2. Eddy detection and tracking algorithms

190   An approach that combines three eddy detection algorithms proposed by Faghmous et al.

191   (2015), Le Vu et al. (2018), and Halo et al. (2014) was developed to detect robust mesoscale

192   eddies in the GoM. The three algorithms represent different approaches of automatic eddy

193   detection and hereafter are referred to as F15, L18, and H14, respectively. In the F15 algorithm,

194   eddies are defined as features of closed-contour SSH with one extremum of SSH. The eddy

195   center is at the location with extremum SSH. The H14 algorithm combines the OW parameter

196   and geometrical properties of SSH. It identifies eddy as contained within a close loop of SSH

197 and dominated by vorticity with the negative OW parameter. The eddy center is the mean

198 position of the identified eddy. The L18 algorithm is a hybrid method based on physical

199 parameters and geometrical properties of the velocity field. The eddy is contained within closed

200 streamlines around an eddy center with a local maximum normalized angular momentum. The

201 differences between the three eddy detection algorithms are that closed SSH contours are used

202 in F15 and H14, while closed streamlines are used in L18. The eddy center is defined differently

203 in the three algorithms and is associated with the SSH extremum location, mean position of

204 eddy, and the local maximum normalized angular momentum in F15, H14, and L18,

205 respectively.

206 Due to the limited resolution of the gridded ADT field, a minimum of 9 pixels was used in the

207 F15 algorithm and a minimum eddy radius of 37 km was used in the other two algorithms. The

208 threshold value of nine pixels was selected in the F15 algorithm because it corresponds to a

209 square area that is occupied by the smallest eddy with a radius of 37 km. Also, a minimum

210 eddy amplitude of 2 cm was applied due to the accuracy of the SSH product (Pujol et al., 2016).

211 The three eddy detection algorithms were implemented to the high-passed ADT field, yielding

212 daily mesoscale eddies. An example of the detected eddies on 20 March 1995, as marked by

213 the black circles in Fig. 2a-c, shows that some eddies can be detected by one algorithm but

214 cannot be detected by the others. The three algorithms, F15, L18, and H14, gave rise to a total

215 of 67016, 65852, and 55309 anticyclonic eddies (AEs), and a total of 93054, 93118, and 86077

216 CEs in the GoM over the examined period, respectively. The daily mean area occupied by AEs

217 in F15, L18, and H14 is $1.91e5$ km^2, $2.42e5$ km^2, and $9.57e4$ km^2, respectively; while the daily

218 mean area occupied by CEs in F15, L18, and H14 is $2.1e5$ km^2, $2.45e5$ km^2, and $1.14e5$ km^2,

219 respectively. The H14 algorithm yields the smallest eddy size and the least eddy number,

220 suggesting the H14 algorithm is more restrictive than the other two algorithms. Moreover, to

221 examine the influence of the spatial filtering that removes the large-scale variability of SSH on

222 eddy detection, we run the eddy detection algorithms on the unfiltered ADT field and compare

223 the eddy numbers with those from the filtered ADT field. A total of 139867, 148309 and

224 125886 eddies are found in F15, L18, and H14, respectively, which are less than 158970,

225 160070 and 141386 eddies when the filtered ADT field is used. The differences of eddy

226 numbers obtained from the filtered and unfiltered ADT fields are from 7% to 12% of the total

227 eddy number. Therefore, the spatial filtering can make eddy features stand out from the large-

228 scale background ADT field.

229
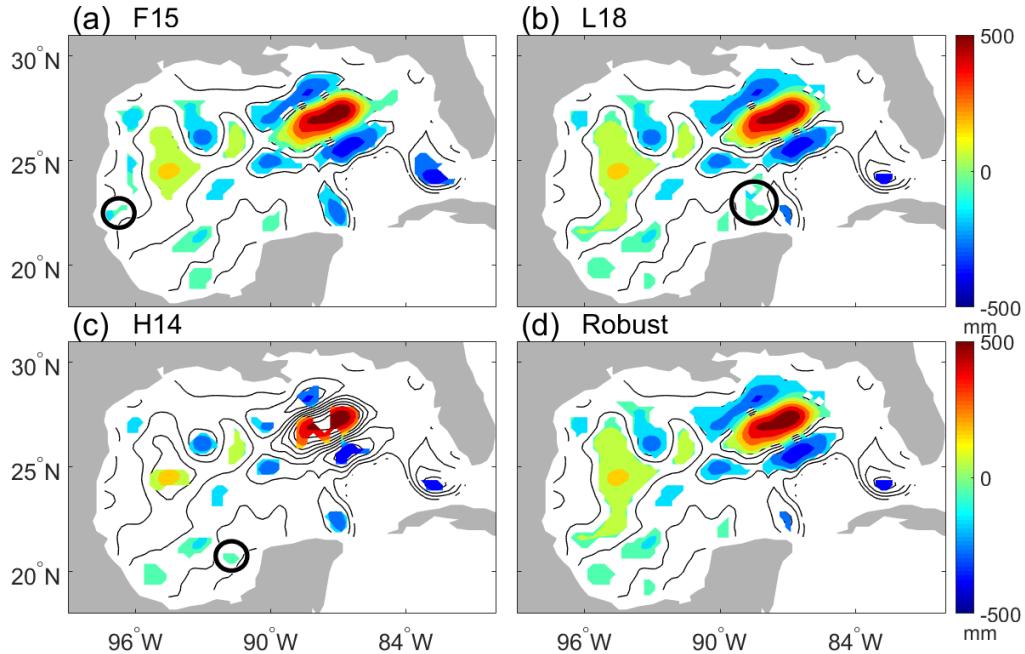
Figure 2: Snapshots of the high-passed ADT (contours) and detected eddies (color shading)

230

231   on 20 March 1995. Eddies were detected by (a) F15 algorithm, (b) L18 algorithm, (c) H14

232   algorithm, and (d) robust detection algorithm. The black circle in (a), (b), and (c) encloses the

233   eddy that was detected by one algorithm but not detected by the other two algorithms.

234

235   We focus on the mesoscale eddies that can be detected by at least two algorithms and define

236   them as the robust eddies in the GoM. Eddies from the most recently developed L18 algorithm

237   were used as basis eddies. For each basis eddy, if common eddy pixels were found in H14 or

238   F15, the eddy was considered robust and kept for further processing. There are 10% of AEs

239   and 7% of CEs detected by L18 that were removed based on the comparison of outputs of the

240   three algorithms. Robust eddies are defined in this way so that we have more confidence in the

241   detected eddies than that given by one algorithm, but they are less restrictive than those given

242   by the H14 method. An example of robust eddies on 20 March 1995 is shown in Fig. 2d.

243   The resulting robust eddies were then tracked with an algorithm that was also used in Le Vu et

244   al. (2018). First, each detected eddy e_i at the last time step t is associated with the closest eddy

245   e_j of the same sign detected at the previous time step t-dt in a given search area. The maximum

246   search distance D_{ij} is then given by $D_{ij} = C(1 + dt)/2 + < R_{max} > (j) + R_{max}(i)$, where $<$

247    $R_{max} > (j)$ is the mean speed-based radius of e_j averaged during the five preceding steps of

248   its track, while $R_{max}(i)$ is the speed-based radius of $e_i(t)$ that corresponds to the eddy radius

249   with maximum mean azimuthal velocity. The speed parameter C is a constant value of 6.5

250   km/day that is one typical upper bound of eddy propagation speed used in the maximum search

251   distance D_{ij} (Le Vu et al., 2018). When no eddies are found in the search area, $e_i(t)$ is identified

252   as a new eddy. When several eddies are found in the search area, e_i will be associated with e_j,

253   which minimizes one cost function:

254   $$\varepsilon_{ij} = \sqrt{\left[\frac{d_{ij}}{D_{ij}(T_c)}\right]^2 + \left[\frac{\Delta R}{<R>(j)+R(i)}\right]^2 + \left[\frac{\Delta Ro}{<Ro>(j)+Ro(i)}\right]^2 + \left(\frac{dt}{2T_c}\right)^2}$$

255   where d_{ij} is the distance between e_i and e_j; $D_{ij}(Tc)$ is the distance D_{ij} at the correlation time

256   (Tc=10 days); ΔR and ΔRo are the radius and the Rossby number difference between e_i and e_j,

257   respectively; $< R > (j)$ and $< Ro > (j)$ are the mean radius and the mean Rossby number of

258   the eddy e_j averaged during the five preceding steps, respectively; the eddy radius is defined as

259   the radius of the circle equivalent to the eddy area. The dimensionless coast function is used to

260   compare physical similarity between eddy pairs. The terms under the root square represent the

261   relative distance between eddy centers, the relative difference between eddy radius, the relative

262   difference between the intensity characterized by Rossby number and the relative difference of

263   temporal separation, respectively. Eddy merging and splitting due to eddy-eddy interactions

264   are considered in this tracking algorithm. Because the temporal correlation scales of gridded

265   ADT data are about 30 days at latitudes of the GoM (Pujol et al., 2016), only eddies with a

266   lifetime greater than 30 days are examined in this study. Although there are eddies with lifetime

267   shorter than 30 days, the gridded SSH data are not independent on timescales shorter than 30

268   days and are not sufficient to detect the short-lived eddies.

269   AEs were further grouped into LCEs and non-LCE AEs. LCEs are AEs that were generated

270   east of 92°W, were dead west of 90°W, translated westward for more than 2 degrees, and had

271   eddy amplitude at the birth time larger than 0.12 m and have a lifespan of more than 60 days.

272   The eddy amplitude was defined as the difference between the SSH on the contour of maximum

273   rotation speed and maximum or minimum SSH in the eddy. Because the LC may experience

274   detachment and reattachment during the formation of LCE, the identified LCE may lose

275   tracking and new eddies were identified. Therefore, AEs that were formed east of 92°W with

276   amplitude larger than 0.2 m and with the distance between eddy center and the LC front being

277   less than 250 km were considered as LCEs as well. The threshold values used in the definition

278   of LCEs were chosen by comparing detected AEs with the SSH maps that show separations of

279   LCEs from the LC. A total of 51 LCE trajectories were found. The larger number of LCE

280   trajectories than that reported in previous studies (e.g., Hall and Leben, 2016) is partially

281   related to temporarily losing track. The separation dates of LCEs with industry names were

282   compared with those reported by Hall and Leben (2016) (Table 1). Separation dates of 28 LCEs

283   are less than 1 month different from those reported by Hall and Leben (2016) (Table 1). There

284   are 376 non-LCE AE trajectories. CEs were further grouped into LCFEs and non-LCFE CEs.

285   Based on the CE trajectories, LCFEs are CEs that have the distance between the eddy center

286   and the LC front be less than 200 km in the first 20 days after the generation. LCFEs defined

287   in this way propagate along the LC front during their lifetimes. Non-LCFEs are CEs that are

288   not identified as LCFEs. There are 297 LCFE trajectories and 447 non-LCFE CE trajectories.

Number	Industry name	Separation date	Separation date (Hall and Leben,	Separation date
1	Whopper	7 July 1993	5 July 1993	2
2	Xtra	16 September	7 September 1993	9
3	Yucatan	22 August	22 August 1994	0
4	Zapp	17 April 1995	18 April 1995	-1
5	Aggie	5 September	7 September 1995	-2
6	Biloxi	13 March	13 March 1996	0
7	Creole	10 August	20 October 1996	-71
8	El Dorado	25 September	26 September	-1
9	Fourchon	6 April 1998	11 February 1998	54
10	Juggernaut	2 October	3 October 1999	-1
11	Millennium	5 April 2001	6 April 2001	-1
12	Pelagic	24 February	26 February 2002	-2
13	Sargassum	7 August	9 August 2003	-2
14	Titanic	19 December	21 December	-2
15	Ulysses	23 August	21 August 2004	2
16	Vortex	9 September	10 September	-1
17	Walker	5 February	5 February 2006	0
18	Xtreme	2 March 2006	2 March 2006	0
19	Yankee	17 September	16 September	1
20	Albert	24 October	12 November	-19
21	Brazos	30 March	7 March 2008	23

22	Cameron	26 June 2008	27 June 2008	-1
23	Darwin	25 February	25 February 2009	0
24	Ekman	26 June 2009	27 June 2009	-1
25	Franklin	9 August	11 August 2010	-2
26	Hadal	23 July 2011	23 July 2011	0
27	Icarus	17 December	20 December	-3
28	Jumbo	10 June 2012	11 June 2012	-1
29	Kraken	25 March	19 May 2013	-55
30	Lazarus	3 November	5 November 2014	-2
31	Nautilus	20 May 2015	14 May 2015	6
32	Olympus	16 October	22 August 2015	55
33	Poseidon	5 April 2016	N/A	N/A
34	Quantum	7 November	N/A	N/A
35	Revelle	6 February	N/A	N/A

289 Note: LCEs reported in Hall and Leben (2016) occurred from 1993 to 2015.

290 **Table 1:** Selected LCE events and their separation dates.

291

292 **3 Results**

293 **3.1 Eddy Trajectories and Propagation**

294 Figure 3 shows the percentages of months when eddy birth, death, and presence were observed
295 over the observation period. LCEs were mostly generated in the northwestern tip of the LC
296 (Fig. 3a), were mostly dissipated in the western GoM, and some of them could reach the
297 western boundary of the GoM (Fig. 3b). They traveled from the east to the southwest in a broad
298 meridional band (Fig. 4a), consistent with the broad paths of LCEs revealed in previous studies
299 (e.g., Hamilton et al., 1999; Vukovich & Crissman, 1986; Vukovich, 2007). Therefore, it is
300 more frequent to observe LCEs in the band from the east to the southwest (Fig. 3c).
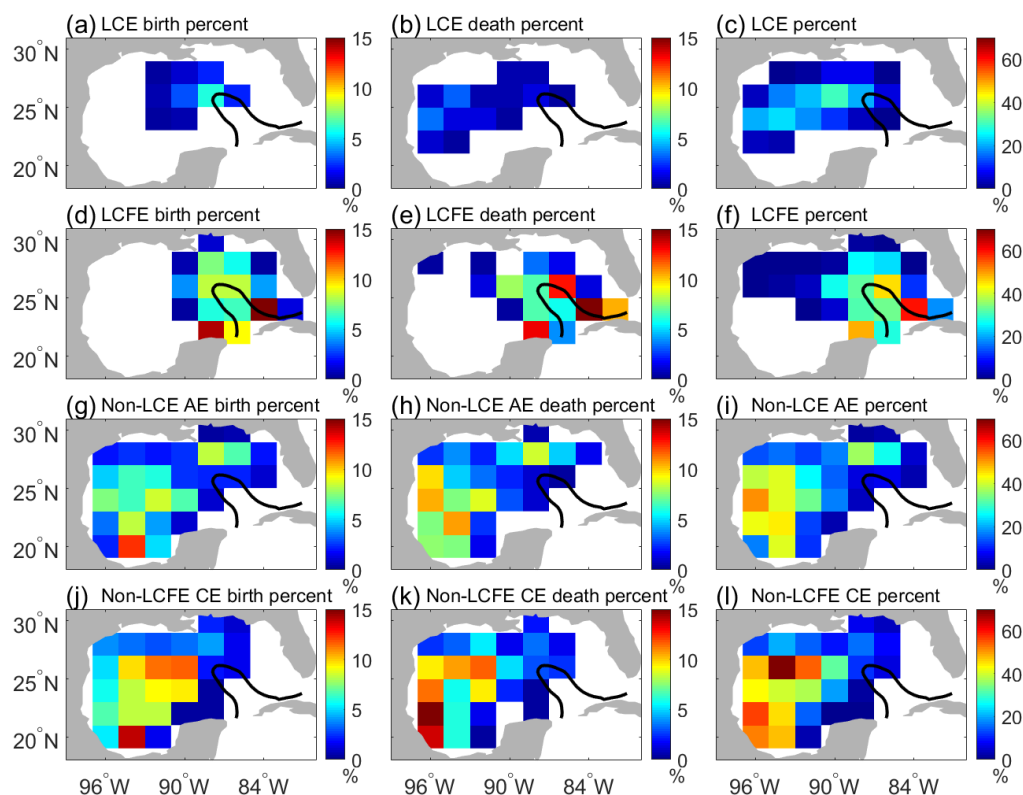
Figure 3: (a, d, g, j) The percentage of months when eddy birth was observed from January 1993 to April 2019. (b, e, h, k) The percentage of months when eddy death was observed. (c, f, i, l) The percentage of months when the presence of eddy was observed. LCEs, LCFEs, non-LCE AEs, non-LCFE CEs are shown in (a-c), (d-f), (g-i), and (j-l), respectively. The black line represents the 25-cm contour of temporal mean SSH anomalies from 1993 to 2019.
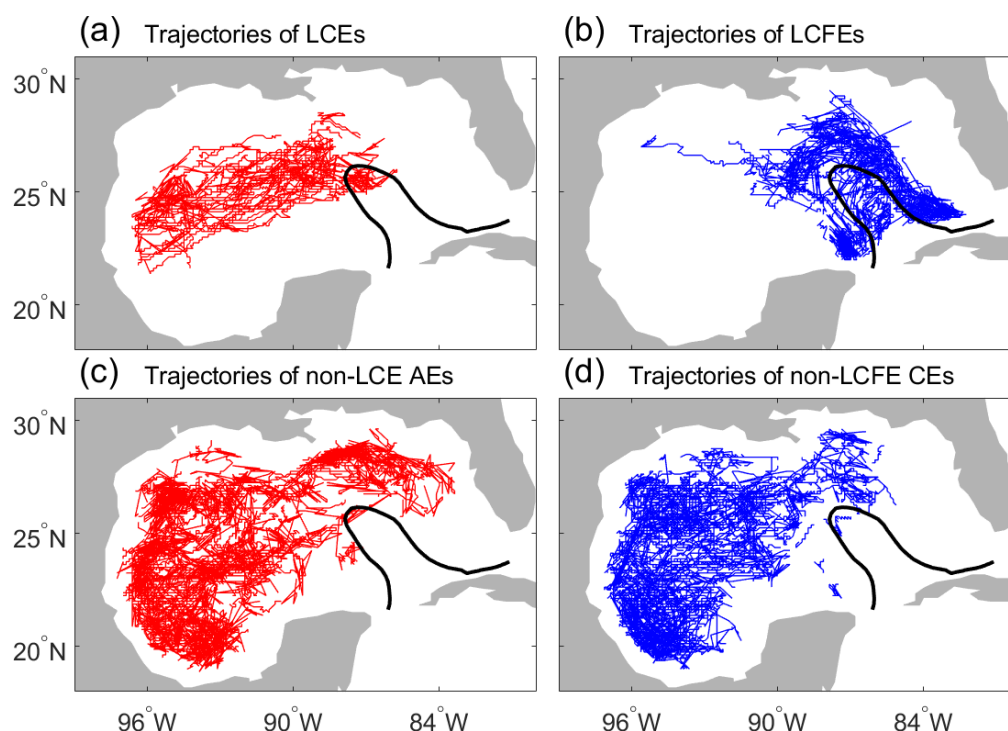
Figure 4: Trajectories of (a) LCEs, (b) LCFEs, (c) non-LCE AEs, and (d) non-LCFE CEs. The thick black line represents the 25-cm contour of temporal mean SSH anomalies from 1993 to 2019.

LCFEs were mostly generated east of Campeche Bank, in the northern and eastern LC (Fig. 3d), and they were more likely to dissipate in the eastern LC (Fig. 3e). LCFEs traveled mainly in the eastern GoM because they were closely tied to the LC (Fig. 4b). LCFEs generated around the Campeche Bank did not travel or lost tracks along the western part of the LC. In the eastern part of the LC, LCFEs traveled along the southward flowing LC. These are consistent with the previous conclusion that LCFE motions along the northern and eastern LC were decoupled from the LCFE motions along the southwestern LC (Donohue et al., 2016a; Donohue et al., 2016b; Hamilton et al., 2016; Walker et al., 2009). In consistence with the LCFE trajectories, LCFEs were most frequently found east of Campeche Bank and in the eastern LC (Fig. 3f). A large fraction of LCFEs has been reported on the eastern flank of the Campeche Bank (Le Hénaff et al., 2014; Jouanno et al., 2016; Zavala-Hidalgo et al., 2003).

324   In contrast to the LCEs and LCFEs that were directly related to the instability of the LC in the

325   eastern GoM, non-LCE AEs and non-LCFE CEs were mostly generated in the western GoM,

326   especially in the central-western GoM and in the Bay of Campeche (Fig. 3g and 3j). They were

327   prone to dissipate along the western boundary of the GoM (Fig. 3h and 3k). The trajectories of

328   non-LCE AEs and non-LCFE CEs are mostly in the western GoM and do not affect the eastern

329   GoM (Fig. 4c-d). In line with the eddy trajectories, the presence frequencies of these eddies are

330   also the highest west of 92°W (Figure 3i and 3l).

331   Although dynamic instabilities of large-scale currents have been reported to be important for

332   the aforementioned spatial pattern of eddy generation (e.g., Chérubin et al., 2006; Donohue et

333   al., 2016a; Jouanno et al., 2016; Maslo et al., 2020; Sturges & Leben, 2000; Yang et al., 2020;

334   Zavala-Hidalgo et al., 2003), the eddy-topography interaction and eddy-eddy interaction could

335   play a role in generating new eddies (Biggs et al., 1996; Frolov et al., 2004; Smith, 1986; Vidal

336   et al., 1992). The eddy-eddy interaction including eddy splitting and merging was also

337   considered in this study following Le Vu et al. (2018). New eddies due to splitting accounts

338   for 15.4% of the total generated eddies. Only 2 LCEs and 16 LCFEs were generated by

339   splitting. However, 80 non-LCE AEs and 82 non-LCFE CEs were generated by splitting and

340   account for 7% of the total generated eddies, respectively. Most non-LCE AEs and non-LCFE

341   CEs due to eddy splitting were scattered in the western GoM (Fig. 5a). In addition to eddy

342   splitting, LCEs could induce eddies along their periphery during the traveling period because

343   of the relatively large current shear around LCEs or when they encounter the western boundary

344   of the GoM. Figure 5b shows the center locations of eddies that were generated along LCE

345   periphery. There are 14 non-LCE AEs and 118 non-LCFE CEs (10% of the total generated

346   eddies) that are likely related to LCEs, showing no particular pattern. Only a small number of

347   CEs were generated along the western boundary of GoM as LCEs arrived there, suggesting

348   that the interaction between LCEs and topography plays a relatively small role in creating new

349   eddies. The dominance of CEs that are possibly induced by LCEs is consistent with the fact

350   that the current shear along LCE periphery is mainly cyclonic.
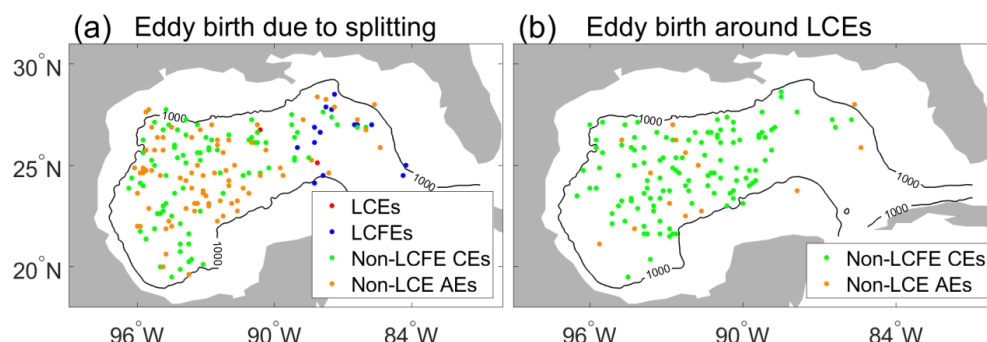
Figure 5: (a) Locations of generated eddies due to splitting. (b) Locations of generated eddies within LCE radius plus 100 km.

Moreover, eddy propagation velocities were estimated by least-squares fitting the positions of eddy centers as a function of time in overlapping 30-day segments of each eddy's trajectory. Figure 6 shows the mean eddy propagation speeds and directions. Mean eddy propagating speeds are highly variable in the GoM. Specifically, LCEs have large traveling speeds in the central-western GoM that can be as large as 5 km/day (Fig. 6a). The mean propagating direction of LCEs is southwestward in the central GoM and bifurcates north and south when LCEs encounter the western boundary of GoM. LCFEs propagate along the LC front and large propagation speeds are found in the eastern part of the LC (Fig. 6b) that are related to the advection of the LC. Non-LCE AEs and non-LCFE CEs have large propagation speeds in the southwest of the GoM and the dominant propagation direction of the two types of eddies is to the west (Fig. 6c-d). The eddy speeds in the western GoM have a similar magnitude as the first-mode Rossby wave propagation speeds (Chelton et al., 2011). However, it should be noted that eddy speeds larger than the first-mode Rossby wave propagation speeds by more than 1 km day^{-1} were also found, which might be related to the background circulation, or in the case of CEs caused by the swirl velocities of a large LCE.
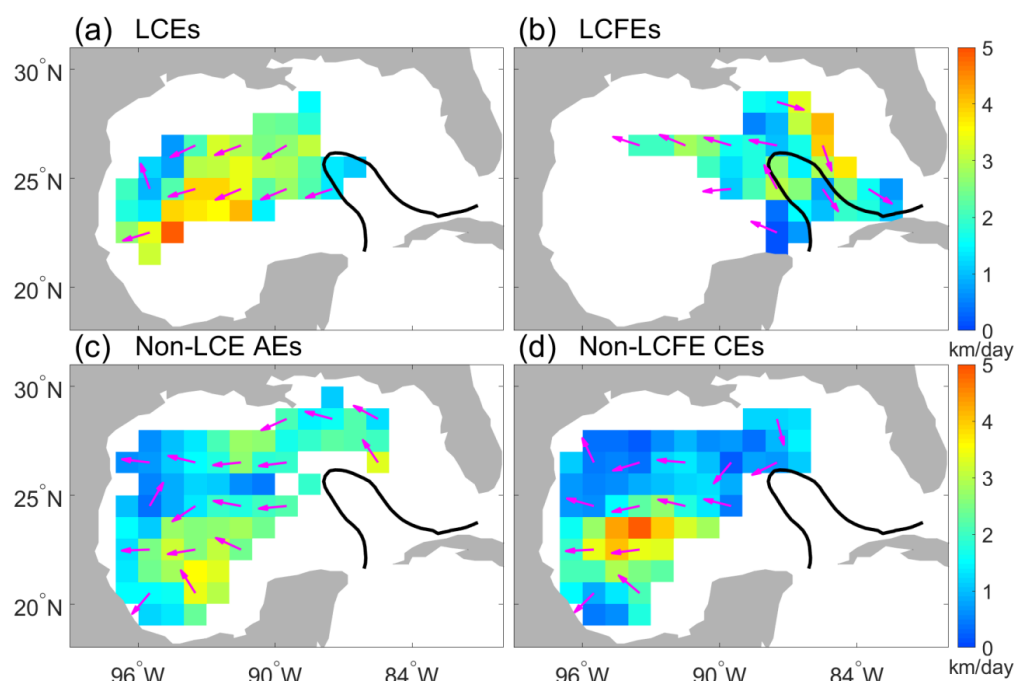
Figure 6: Mean eddy propagation speeds (color shading) and directions (magenta arrows) for (a) LCEs, (b) LCFEs, (c) non-LCE AEs, and (d) non-LCFE CEs. The thick black line represents the 25-cm contour of temporal mean SSH anomalies from 1993 to 2019.

3.2 Basic Eddy Characteristics

Distributions of some basic eddy characteristics derived from the mean values along eddy trajectories are presented in Fig. 7a-e, and the distribution of eddy lifetime is shown in Fig. 7f. Apparent differences between the four types of eddies appear in their amplitude, scale, relative vorticity, maximum rotational speed, and advective nonlinearity (Fig. 7a-e). LCEs have the largest mode values of eddy amplitude, LCFEs have a smaller eddy amplitude, and non-LCE AEs and non-LCFE CEs have the smallest mode values of eddy amplitude (Fig. 7a). The distributions of the eddy scale, defined as the radius with the maximum rotational speed (Chelton et al., 2011), show that LCEs have the largest scale and that the other three types of eddies have smaller and similar mode values of eddy scale (Fig. 7b). The distributions of the relative vorticity, maximum rotational speed, and advective nonlinearity show that LCEs and LCFEs have larger magnitudes of mode values than those of non-LCE AEs and non-LCFE CEs (Fig. 7c-e). The nonlinearity of eddy was assessed with the advective nonlinearity parameter,

388   U/C, where U is the maximum rotational speed and C is the translation speed of eddy. Eddies

389   with U/C > 1 can advect trapped fluid within the eddy interior when they translate (Chelton et

390   al., 2011; Flierl, 1981). All the nonlinearity parameters averaged over the eddy trajectories are

391   larger than 1, confirming that eddies in the GoM are highly nonlinear. Nearly 25.1% of AEs

392   have a lifetime longer than 100 days. About 16.7% of CEs can live longer than 100 days (Fig.

393   7f).

394
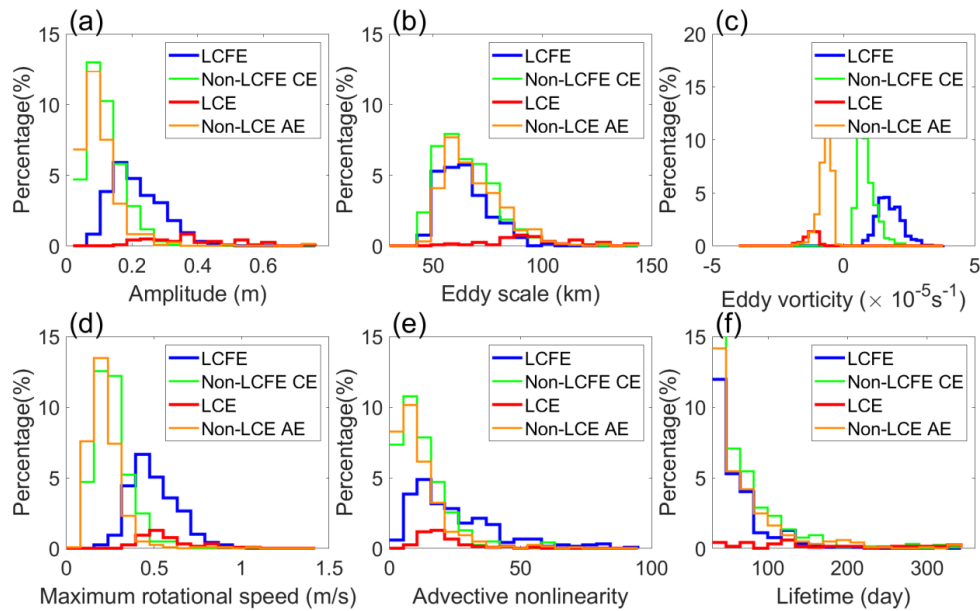
395   **Figure 7:** Histograms of basic eddy characteristics: (a) amplitude (m), (b) eddy scale (km), (c)

396   eddy relative vorticity (s⁻¹), (d) maximum rotational speed (m/s), (e) advective nonlinearity

397   (unitless), (f) lifetime (day).

398

399   Because the temporal correlation scale of gridded ADT data is about 30 days, the obtained

400   eddy amplitude, scale, and maximum rotational speed were mapped into monthly data on two-

401   degree grids. To illustrate their spatial distributions, the temporal mean eddy characteristics on

402   spatial grids are shown in Fig. 8. Eddy characteristics within the LC are not considered in this

403   study because SSH fields within the LC region were removed. Mean values of the LCE

404   amplitude, scale, and maximum rotational speed are large northwest of the LC where LCEs

405   were shed from the LC (Fig. 8a-c) and are much larger than those of the other three types of

406   eddies. The larger amplitude of LCEs is expected due to their larger size even with a rotational

407   speed comparable to smaller eddies. LCFEs have relatively large amplitude and rotational

408   speed in the southeastern part of the LC (Fig. 8d and 8f), in agreement with previous estimates

409   that LCFEs have larger amplitude and rotational speed in the northern and eastern side of the

410   LC than on the western side (e.g., Le Hénaff et al., 2014). Compared to the eddy amplitude and

411   rotational speed, the LCFE scale is relatively uniform (Fig. 8e). In contrast to LCEs and LCFEs,

412   non-LCE AEs and non-LCFE CEs show relatively small spatial variations of amplitude, scale,

413   and rotational speed (Fig. 8g-l). The spatial patterns of the eddy amplitude, scale, and

414   maximum rotational speed are not likely related to the eddy number distributions (Fig.s 3 and

415   8).

416
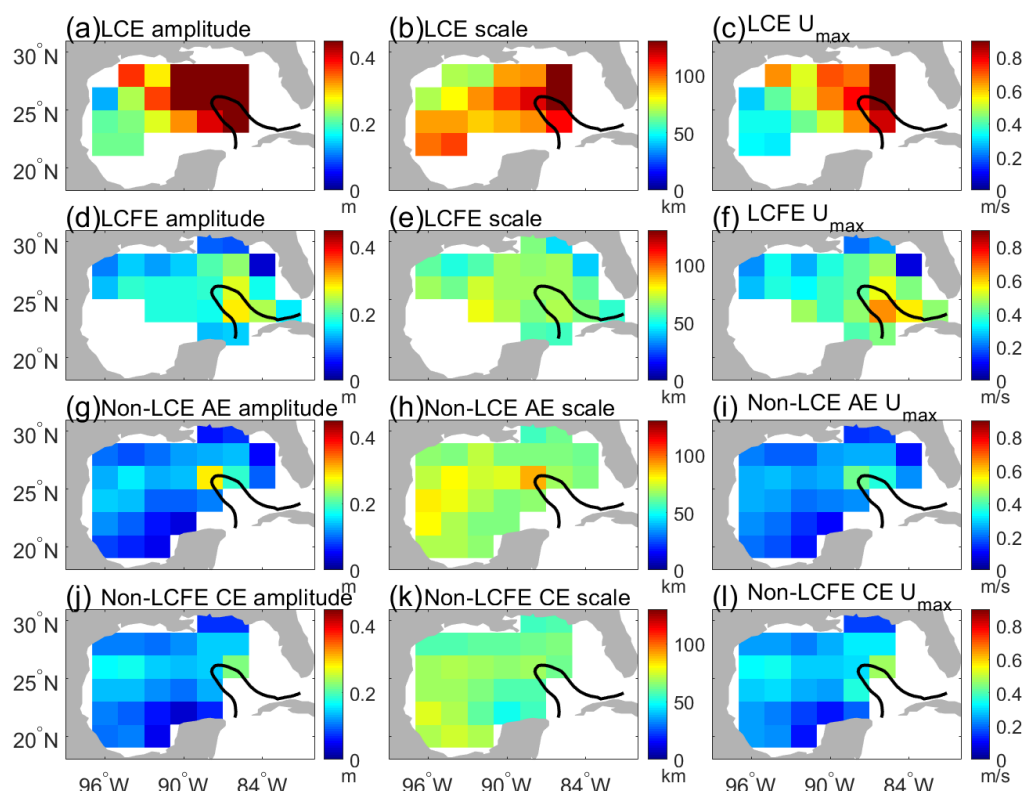
Figure 8: Eddy mean amplitude (m) for (a) LCEs, (d) LCFEs, (g) non-LCE AEs, and (j) non-LCFE CEs. Eddy mean scale (km) for (b) LCEs, (e) LCFEs, (h) non-LCE AEs, and (k) non-LCFE CEs. Eddy mean maximum rotational speed (m/s) for (c) LCEs, (f) LCFEs, (i) non-LCE AEs, and (l) non-LCFE CEs. The black line represents the 25-cm contour of temporal mean SSH anomalies from 1993 to 2019.

422

3.3 Monthly Climatology of Eddies

Monthly climatology of eddy number was obtained and expressed in percentage of the total generated eddies (Fig. 9). The seasonal peak of LCE birth in September and the secondary peak in February are observed (Fig. 9a), which are consistent with that reported by Hall and Leben (2016). The seasonal variation of LCEs is the smallest compared to the other three types of eddies and is not significant at the 95% confidence level. However, Hall and Leben (2016) showed that the seasonal peak of LCE separation in August and September is significant, which could be related to the seasonal variability of wind patterns in the Caribbean Sea and Gulf of Mexico (Chang & Oey, 2012, 2013). In this study, because LCEs show different birth number and date (Table 1) resulting from uncertainties due to the detachment, reattachment of LCEs and eddy splitting (Fig. 5a), the seasonality of LCE separation is not significant. The nonsignificant seasonal variability of LCE separation may be partially related to the physical processes that do not have apparent seasonal variability but can affect the LCE separation. For example, fluctuations such as mesoscale eddies from the Caribbean Sea (Huang et al., 2021; Murphy et al., 1999; Oey et al., 2003) can influence the LCE separation.
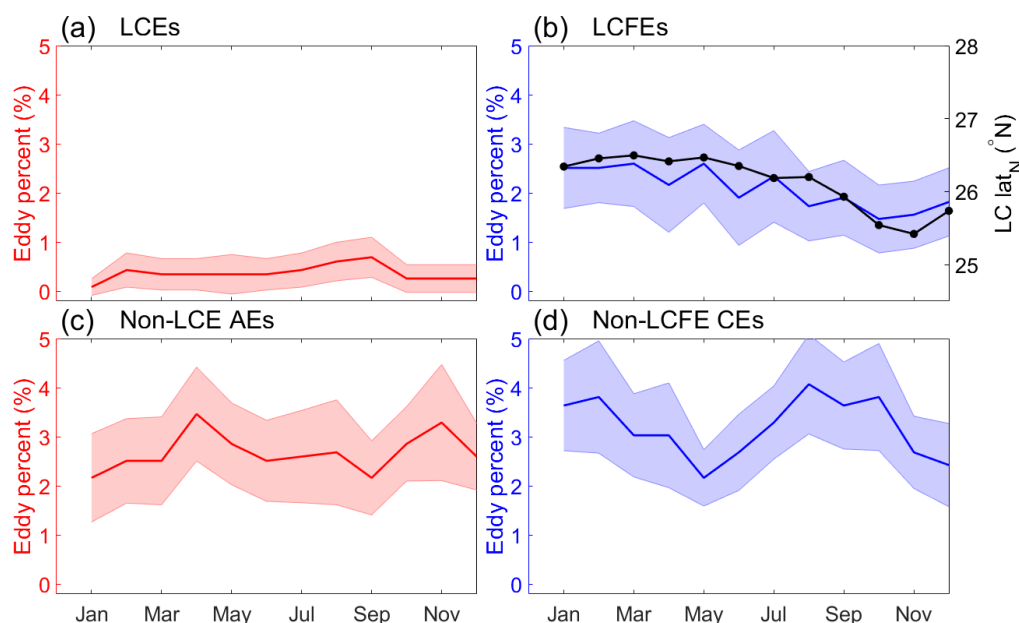
Figure 9: (a) The percentage of birth number of LCEs relative to the total eddy birth number. (b) The percentage of birth number of LCFEs relative to the total birth number. The black line in (b) represents the monthly climatology of the LC position. (c) The percentage of birth number of non-LCE AEs relative to the total birth number. (d) The percentage of birth number

443   of non-LCFE CEs relative to the total birth number. The shading denotes the 95% confidence

444   level represented by two times standard deviation of eddy percentage in each month.

445

446   Compared to LCEs, more LCFEs are observed and the birth number of LCFEs is larger in

447   January to July than in October to December (Fig. 9b). The magnitude of the seasonal variation

448   of LCFEs is close to 1% of the total eddy birth number, but it is still not significant at the 95%

449   confidence level. Because LCFEs are generated along the LC peripheral, the extent of northern

450   penetration of the LC may be one important factor for the LCFE generation. The seasonal

451   variation of the northern boundary of the LC is shown to have a similar variation as that of

452   LCFEs (Fig. 9b). Hamilton et al. (2014) also showed that altimeter-derived LC northern-

453   boundary latitude is relatively high from January through about July and low in September and

454   October. The more northward the LC penetrates, the more LCFEs are generated.

455   The seasonal variations of non-LCE AEs and non-LCFE CEs are relatively large, but

456   differences of eddy number between most months are not significant at the 95% confidence

457   level due to large uncertainties (Fig. 9c-d). The number of non-LCFE CEs is small in May and

458   December and is large in February and August (Fig. 9d), indicating a biannual variability.

459   Compared to the non-LCFE CEs, the seasonal variation of non-LCE AEs has a different phase

460   and a smaller amplitude (Fig. 9c). Both the background currents and eddy-eddy interaction

461   might be important for the seasonality of the two types of eddies. Figure 10 shows the monthly

462   climatology of the eddy numbers of non-LCE AEs and non-LCFE CEs that were induced by

463   eddy splitting and LCEs. The seasonal variations of AEs and CEs induced by splitting and

464   LCEs are small and are not significant at the 95% confidence level. It should be noted that their

465   seasonal variations are much smaller and more random than those shown in Fig. 9c-d.

466   Therefore, the seasonal variations of non-LCE AEs and non-LCFE CEs (Fig. 9c-d) are not

467   related to eddy-eddy interaction represented by eddy splitting and the effect of LCEs and could

468   be likely related to the background currents.

469
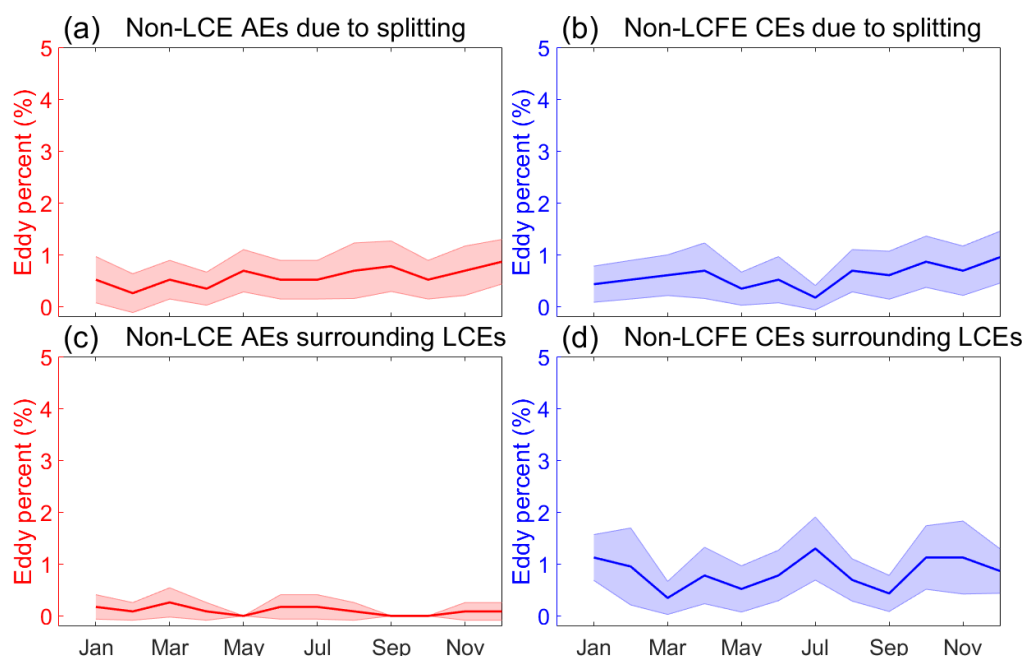
Figure 10: (a) The percentage of non-LCE AEs generated due to splitting relative to the total
generated eddies. (b) The percentage of non-LCFE CEs generated due to splitting relative to
the total generated eddies. (c) The percentage of non-LCE AEs generated within LCE radius
plus 100 km relative to the total generated eddies. (d) The percentage of non-LCFE CEs
generated within LCE radius plus 100 km relative to the total generated eddies. The shading
denotes the 95% confidence level represented by two times standard deviation of eddy
percentage in each month.

To further show spatial patterns of the monthly climatology of generated eddies, the locations
of eddy centers were mapped on two-degree grids (Fig. 11). Figure 11a-d shows the generation
locations of LCEs and the mean position of the LC in February, May, August, and November.
The LC has a more northward penetration in February and May than in August and November
but more LCEs are formed at the northwestern tip of the LC in August than in other months,
suggesting no clear linkage between the generation of LCEs and the LC northern boundary can
be built. However, more LCFEs can be found in the northern LC in February and May when
the LC makes more penetration than in August and November when the LC makes less
penetration (Fig. 11e-h). Therefore, a more northward penetration of the LC favors the
generation of LCFEs.
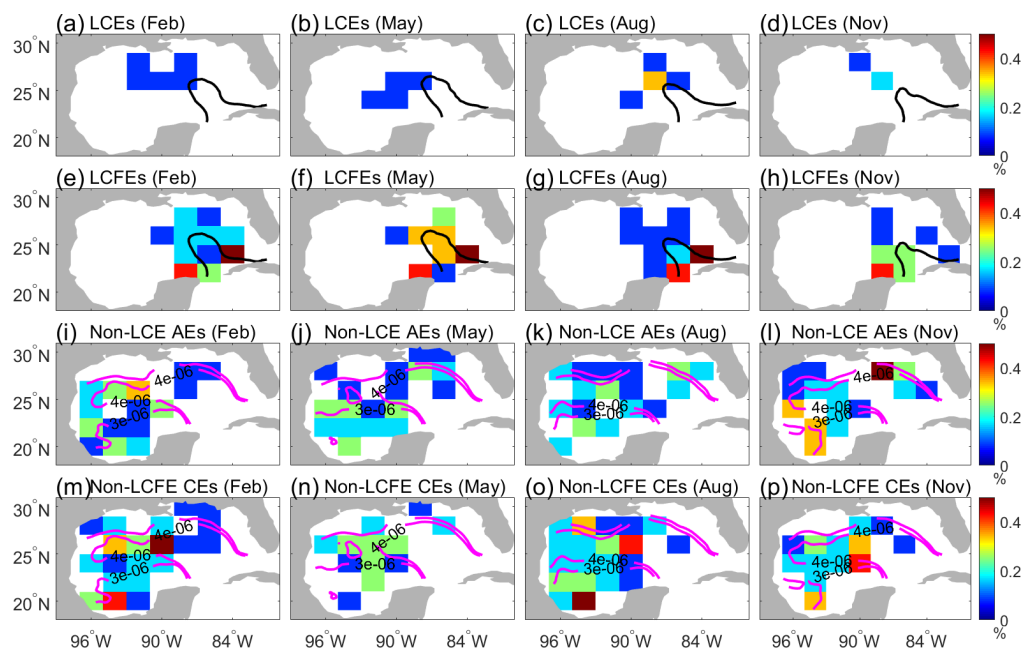
Figure 11: (a-d) LCE percentage relative to the total generated eddies in (a) February, (b) May, (c) August, and (d) November. (e-h) LCFE percentage relative to the total generated eddies in (e) February, (f) May, (g) August, and (h) November. (i-l) Non-LCE AE percentage relative to the total generated eddies in (i) February, (j) May, (k) August, and (l) November. (m-p) Non-LCFE CE percentage relative to the total generated eddies in (m) February, (n) May, (o) August, and (p) November. The black lines in (a-h) represent the mean position of the LC in February, May, August, and November, respectively. The magenta lines in (i-p) represent the monthly climatology of current speed gradient in February, May, August, and November, respectively.

Compared to LCEs and LCFEs that are closely related to the LC, the generation of non-LCE AEs and non-LCFE CEs is scattered over the whole GoM and is mainly in the western GoM (Fig. 11i-p). The contours of current speed gradient in Fig. 11i-p indicate the position of strong background currents. The generation locations of eddies tend to move with the seasonal movement of strong currents, from which eddies may obtain energy. However, non-LCE AEs do not show a significant change in the birth number between different months, which is also indicated in Fig. 9c. It is noted that the number of non-LCFE CEs is more likely related to the strength of the background currents (Fig. 11m-p). More non-LCFE CEs were generated along

507   the boundary of strong currents in February and August and fewer non-LCFE CEs were
508   generated in May and November. Since most non-LCE AEs and non-LCFE CEs were
509   generated in the western GoM, the current speeds and directions in the western GoM in the
510   four months are highlighted and shown in Fig. 12. The background currents in western GoM
511   are stronger in February and August than in May. The mean currents in the central western
512   GoM flow westward approximately at 22-23°N and eastward at 25-27°N, forming an
513   anticyclonic circulation pattern. It is noted that the currents change direction with season along
514   the western boundary. Therefore, the non-LCFE CEs were more likely formed along the
515   periphery of the strong anticyclonic circulation pattern in the western GoM. It is noted that the
516   eddy generation location varies within the strong-current region and sometimes few eddies are
517   generated. One possible reason is that the large-scale background current can influence the
518   eddy generation but is not the only factor that determines the eddy generation location and
519   other factors such as wind stress play some role.
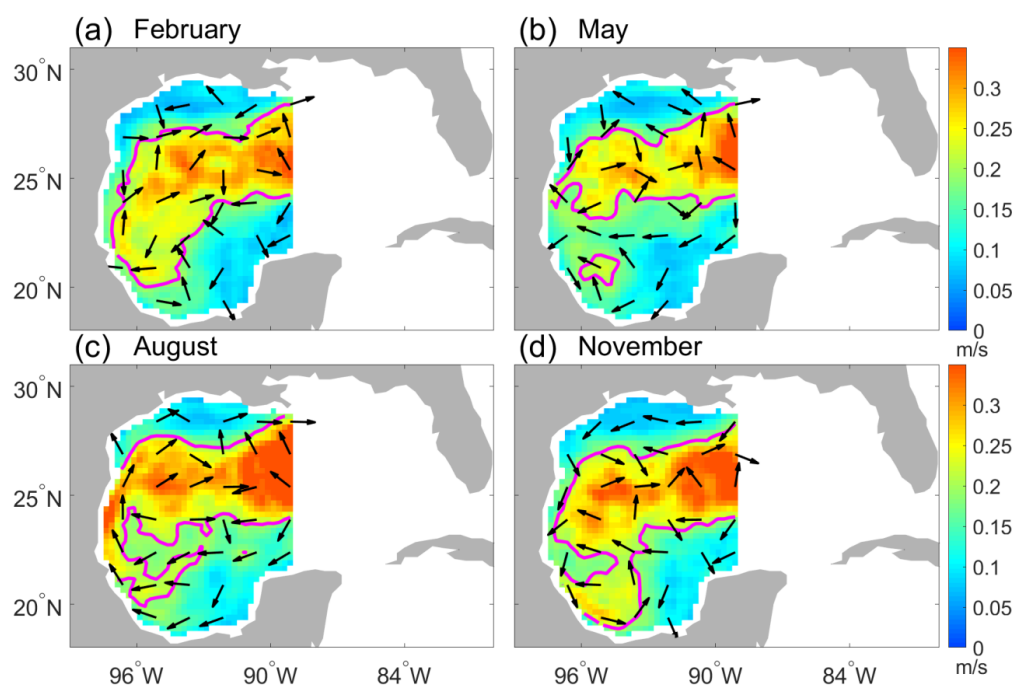
520
521   **Figure 12**: Current speeds (m/s, color shading) climatology and mean current direction
522   (arrows) west of 89°W in the GoM in (a) February, (b) May, (c) August, and (d) November.
523   The magenta contour denotes the current speed of 0.2 m/s.

524

525 In addition to the seasonality observed in the eddy birth number, the seasonal variability of
526 eddy amplitude at the time of eddy birth was examined. The monthly climatology of median
527 eddy amplitude is presented in Fig. 13. Since eddy amplitude is not normally distributed,
528 median eddy amplitude was used to mitigate the potential influence of amplitude outliers.
529 Compared to the seasonal variability of eddy number, the seasonal variability of eddy
530 amplitude is less apparent. LCEs and LCFEs have relatively larger monthly variations and
531 uncertainties than non-LCE AEs and non-LCFE CEs. It should be noted that the seasonal
532 variation of LCE amplitude may not be reflected from the relatively short record because it was
533 estimated from a relatively small number of LCEs that is less than 6 in most months.

534
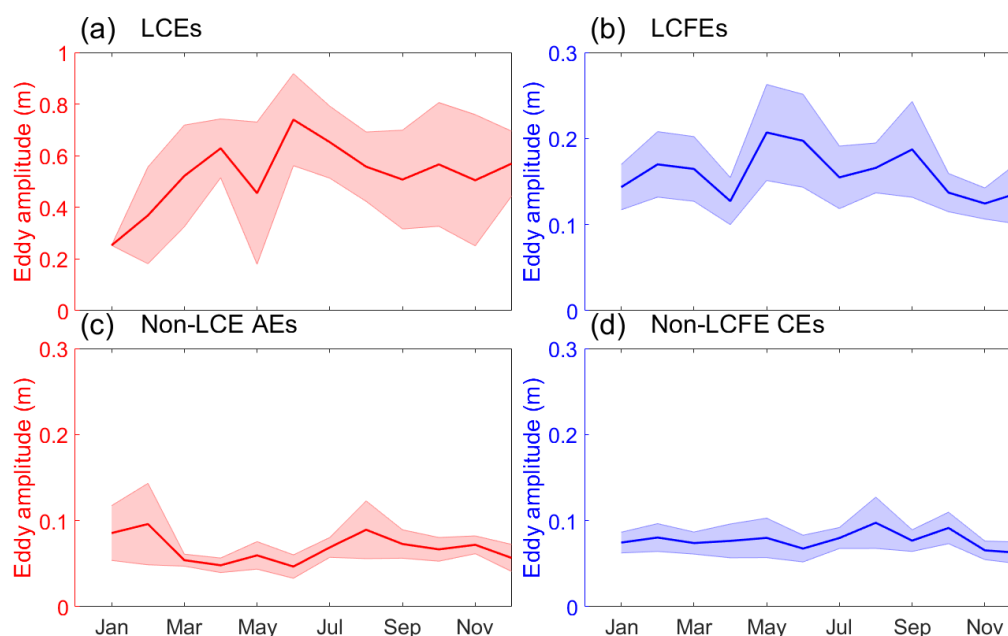
535 **Figure 13:** Monthly climatology of eddy amplitude of (a) LCEs, (b) LCFEs, (c) non-LCE AEs,
536 and (d) non-LCFE CEs whey they were generated. The shading denotes the 95% confidence
537 level represented by two times standard deviation of amplitude.

538

539 **3.4 Low-frequency Variability of Eddies**

540 To examine the low-frequency variability of eddies, annual variations of eddy birth number
541 and amplitude were obtained. Figure 14 shows the annual variations of the birth number of
542 eddies. The generation of LCEs is relatively rare and shows a weak variability (Fig. 14a). The
543 other three types of eddies indicate a larger variability. A linear regression model that includes

544   a linear trend, ENSO index, NAO index, and AMM index was applied to the annual eddy

545   number. An increasing number of LCEs over 2001-2010 has been found in previous studies

546   (Lindo-Atichati et al., 2013; Vukovich, 2012). Nevertheless, no long-term variability of other

547   types of eddies has been reported. The linear trends of the annual birth number of LCEs,

548   LCFEs, non-LCE AEs, and non-LCFE CEs from 1993 to 2018 are $3.5\times10^{-2} \pm 3.3\times10^{-2}$ ($\pm1\sigma$)

549   year^{-1}, -0.2 ± 0.17 ($\pm1\sigma$) year^{-1}, -0.06 ± 0.11 ($\pm1\sigma$) year^{-1}, and 0.05 ± 0.11 ($\pm1\sigma$) year^{-1},

550   respectively. These linear trends are not significant at the 95% confidence level. LCFEs have

551   the largest decreasing trend that is not significant, which is likely related to the negative trend

552   of the northern boundary of the LC that is $-1.7\times10^{-2} \pm 1.7\times10^{-2}$ ($\pm1\sigma$) degree year^{-1}. Regression

553   coefficients of the three climate indices are not significant as well. For the four types of eddies,

554   the coefficients of determination of the three climate indices are less than 0.08. Therefore, only

555   a small portion of eddy number variance can be explained by the three climate modes,

556   indicating that the role of the remote climate variability in changing the eddy activity in the

557   GoM is relatively small or cannot be detected from the linear model.

558
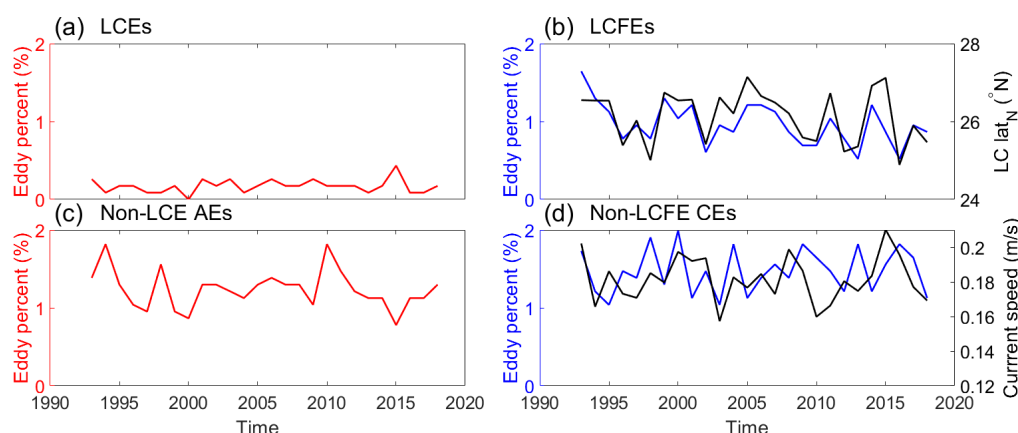
559   **Figure 14:** Annual number of generated (a) LCEs, (b) LCFEs, (c) non-LCE AEs and (d) non-

560   LCFE CEs and is expressed as percentage of the total new eddy from 1993 to 2018. The black

561   line represents the annual mean northern boundary (°N) of the LC in (b) and the annual mean

562   current speed (m/s) in the western GoM in (d).

563

564   In the eastern GoM, the low-frequency variability of eddy number is likely related to that of

565   the LC. Figure 14b shows the annual mean variation of the northern boundary position of the

566   LC that particularly follows the variation of LCFEs. Correlation between the birth number of

567   LCEs and the northern boundary position of the LC is small and not significant (Table 2),

568 therefore, the extent of LC penetration plays a relatively small role in the separation of LCEs.
569 However, the LCFE number and the northern boundary position of the LC are correlated with
570 a significant correlation of 0.76, indicating that the LCFE number increases with the northward
571 penetration of the LC on the interannual to multidecadal time scale (Table 2). The extent of
572 northward penetration of the LC is important for the LCFE generation although previous
573 studies have shown that perturbations coming from the Caribbean Sea (Huang et al., 2013) and
574 the topography of the northern Campeche (Chérubin et al., 2006) also contribute to the eddy
575 activity along the western edge of the LC.

	LCE number	LCFE number	LCE amplitude	LCFE amplitude
LC northern boundary	0.38	**0.76**	-0.17	-0.26

576 **Table 2:** Correlations between the annual number and amplitude of LCEs and LCFEs with the
577 annual mean northern boundary of the LC. The value in bold is significant at the 95%
578 confidence level.

579

580 For the non-LCE AEs and non-LCFE CEs, the eddy numbers also show large annual mean
581 variations (Fig. 14c-d). Since the background current strength could be important in affecting
582 the low-frequency eddy activity (Chen et al., 2011), birth numbers of non-LCE AEs and non-
583 LCFE CEs, which were mostly formed in the western GoM, were compared with the surface
584 current speed averaged in the western GoM (Fig. 14d). The non-LCE AE number and the non-
585 LCFE CE number are correlated and anticorrelated with the mean surface current speed in the
586 western GoM respectively, but the correlation values are not significant at the 95% confidence
587 level (Table 3).

	Non-LCE AE number	Non-LCFE CE number	Non-LCE AE amplitude	Non-LCFE CE amplitude
Current speed in WGOM	-0.42	0.33	0.47	0.47

588 **Table 3:** Correlations between the annual number and amplitude of non-LCE AEs and non-
589 LCFE CEs with the annual mean current speed in the western GoM.

590

591   In addition to the influence of background currents, the eddy-eddy interaction that includes

592   eddy splitting and eddy formation related to LCEs is considered as well. The annual mean

593   variability of eddies due to eddy-eddy interaction is relatively weak. After removing the eddies

594   induced by eddy splitting and LCEs, the correlations between non-LCE AE number, non-LCFE

595   CE number, and the mean surface current speed in the western GoM are -0.38 and 0.32,

596   respectively. Those numbers are similar to -0.42 and 0.33 shown in Table 3. The eddy-eddy

597   interaction has little effect on the relationship between western eddies and the background

598   flows. Since a much smaller number of eddies due to eddy splitting and LCEs are found along

599   the western boundary (Fig. 5) where LCEs could interact with the topography (e.g., Vidal et

600   al., 1992), the eddy-topography interaction is not important for the low-frequency variability

601   of eddies.

602   The relationship between the eddy number and the strength of the circulation in the western

603   GoM was further examined with composite analysis. The mean current speeds and flow

604   directions in the western GoM during the periods with more non-LCFE CEs and fewer non-

605   LCFE CEs are shown in Fig. 15. When the annual number of non-LCFE CEs is one standard

606   deviation larger than the average eddy number, strong mean anticyclonic circulation is

607   observed in the western GoM. When the annual number of non-LCFE CEs is one standard

608   deviation smaller than the average eddy number, weak mean anticyclonic circulation is

609   observed in the western GoM. However, over the period with more non-LCE AEs weak mean

610   anticyclonic circulation is observed in the western GoM. Over the period with fewer non-LCE

611   AEs strong mean anticyclonic circulation is observed in the western GoM. Therefore, the

612   strength of the background circulation could play a role in influencing the low-frequency

613   variability of eddy number.
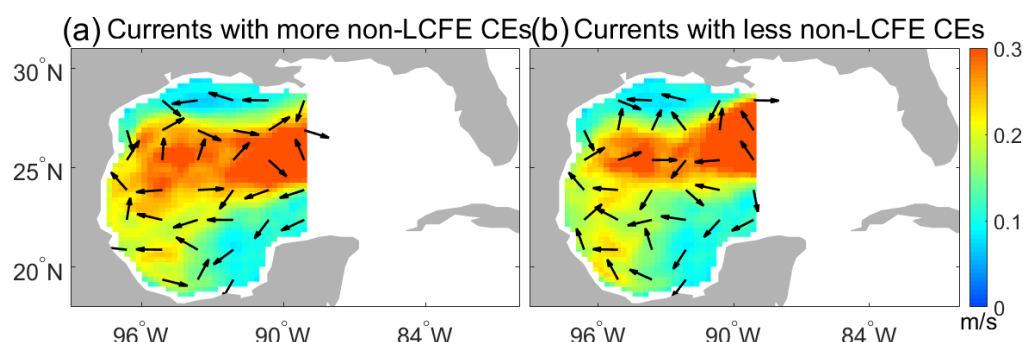
615   **Figure 15**: Composite of current speeds west of 89°W in the GoM (a) during the period with

616   more generated non-LCFE CEs (annual number of non-LCFE CEs is larger than mean value

617   plus one standard deviation), and (b) during the period with fewer non-LCFE CEs (annual

618   number of non-LCFE CEs is smaller than mean value minus one standard deviation). Arrows

619   denote the mean current direction.

620

621   Eddy amplitude in the GoM exhibits low-frequency variability as well. To mitigate the

622   potential influence of amplitude outliers, the median amplitude of eddies at the time of birth in

623   each year was selected for the analysis of the low-frequency variability of eddy amplitude (Fig.

624   16). LCEs show the largest annual variation of eddy amplitude (Fig. 16a) that was obtained

625   from a small number of LCEs (Fig. 14a). The amplitude variation of LCFEs is weaker than that

626   of LCEs but is larger than those of non-LCE AEs and non-LCFE CEs (Fig. 16b). The variations

627   of LCE and LCFE amplitude are not closely related to the northern boundary of the LC with

628   small correlations (Table 2), suggesting the extent of the LC penetration is not an important

629   factor for the eddy amplitude at the time of birth. For non-LCE AEs and non-LCFE CEs, the

630   eddy amplitude at the time of birth seems to be related to the strength of background currents

631   in the western GoM (Fig. 16c-d) but with a nonsignificant positive correlation of 0.47 (Table

632   3).

633
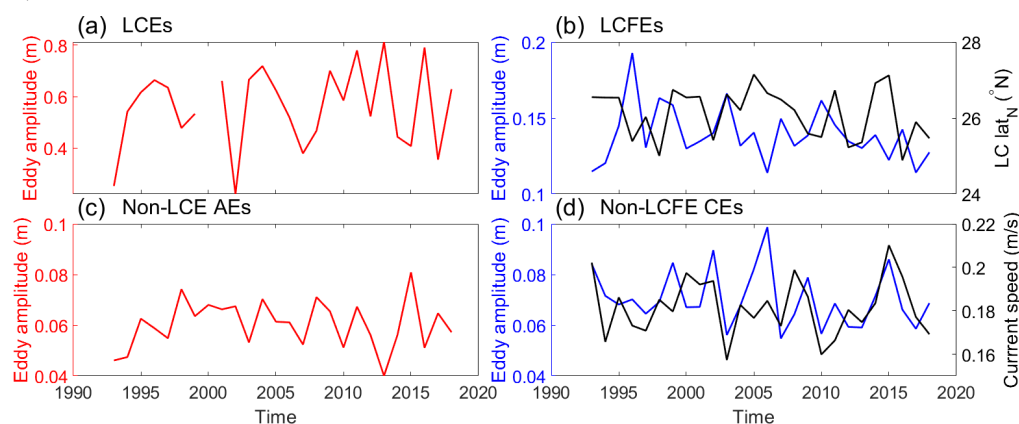
634   **Figure 16**. Annual median amplitude (m) of the (a) LCEs, (b) LCFEs, (c) non-LCE AEs and

635   (d) non-LCFE CEs when they were generated. The black line represents the annual mean

636   northern boundary (°N) of the LC in (b) and the annual mean current speed (m/s) in the western

637   GoM in (d).

638

4 Conclusions and Discussions

In this study, we present characteristics of the robust mesoscale eddies in the GoM, including their spatial distributions, propagation features, seasonal and low-frequency variabilities. As expected, many eddy characteristics in the eastern GoM are closely related to the LC, which sheds large and strong LCEs and develops small-scale LCFEs (e.g., Brokaw et al., 2020; Le Hénaff et al., 2014). Compared to LCEs and LCFEs, non-LCE AEs and non-LCFE CEs are mainly formed in the central-western GoM, tend to dissipate along the western boundary, and have smaller amplitude, relative vorticity magnitude, rotational speed, and nonlinearity. Among LCEs, LCFEs, non-LCE AEs, and non-LCFE CEs, only LCEs can travel a long distance from the eastern to the western GoM, as observed from other datasets (e.g., Vukovich 2007). Temporally mean propagation speeds are high in the eastern part of the LC and the southwestern GoM.

The temporal variability of eddy occurrence and amplitude, which is less reported in the literature, shows manifest spatial patterns and dramatic differences between LCEs, LCFEs, non-LCE AEs, and non-LCFE CEs. This study indicates a biannual variability of LCE separation with large uncertainties that is similar to that found in a shorter record by Hall & Leben (2016). However, the seasonality in LCE formation is not significant, while Hall and Leben (2016) suggested that the seasonal peak in LC eddy separation events in August and September was significant. The seasonal variabilities of birth numbers of the other three types of eddies are also not significant at the 95% confidence level. Nevertheless, LCFEs and non-LCFE CEs show more apparent seasonal patterns than LCEs and non-LCE AEs. More LCFEs are observed from January to July, while more non-LCFE CEs are found in February and August. Fewer LCFEs are observed from August to December, while fewer non-LCFE CEs are found in May and December. Moreover, the seasonal variability of eddy amplitude at the time of eddy birth is more random than that of eddy number. Similar to the temporal mean characteristics, the seasonal variability of eddy amplitude of LCEs and LCFEs at the time of eddy birth is much larger than that of non-LCE AEs and non-LCFE CEs. On the low-frequency time scale, although an increasing number of LCEs in the decade 2001-2010 has been found in previous studies (Lindo-Atichati et al., 2013; Vukovich, 2012), the linear trends of LCEs and other three types of eddies obtained in this study are not significant at the 95% confidence level.

The seasonal and low-frequency variabilities described above could be closely related to the large-scale background circulations such as the LC, eddy-eddy interaction, and eddy-

672   topography interaction. On the seasonal time scale, the extent of northward penetration of the

673   LC is important for LCFE generation but not for their amplitude. The position and strength of

674   background currents in the western GoM are likely important for the formation of non-LCFE

675   CEs and non-LCE AEs that are mostly formed in the western GoM. On the low-frequency time

676   scale (interannual to multidecadal), LCFE number is related to the extent of northward

677   penetration of the LC in the eastern GoM. In the western GoM, the surface circulation strength

678   could be important for the low-frequency variability of eddy occurrence and amplitude, which

679   is also found in other oceans (e.g., Chen et al., 2011). In contrast, the eddy-eddy interaction

680   that includes eddy splitting and the effect of LCEs and the eddy-topography interaction give

681   rise to a relatively small number of eddies and play a small role in the temporal variability of

682   eddies.

683   Although climate change and variability may be altering the oceanic conditions in the GoM

684   (e.g., Rodriguez-Vera et al., 2019), the linear trend of eddy occurrence and the low-frequency

685   variability related to climate modes such as NAO, AMM and ENSO are not significant in the

686   current record.

687   Note that eddy characteristics obtained in this study may include uncertainties caused by

688   drawbacks in eddy detection and tracking algorithms despite a combination of three different

689   eddy detection algorithms. For instance, geometrical properties in detection algorithms are

690   sensitive to interval searching for closed contours (Lian et al., 2019). With the increasing

691   knowledge of mesoscale eddies and improved eddy detection and tracking algorithms, more

692   robust eddies will be obtained in future studies. In addition to the limitation of eddy detection

693   and tracking algorithms, satellite sampling could affect the detection of the mesoscale activity

694   (Le Traon and Dibarboure, 1999) and the LC statistics (Dukhovskoy et al., 2015). The allsat

695   ADT product was derived from a varying number of altimeters and was useful for examining

696   the influence of satellite sampling on eddy detection. Mesoscale eddies were detected with the

697   algorithm developed by Le Vu et al. (2018) from the allsat ADT product and were compared

698   with those detected from the twosat ADT. From 1 January 1993 to 31 December 1999 when

699   twosat and allsat ADT data were mainly derived from 2 alitmeters, 41388 and 41343 eddies

700   were detected from the twosat and allsat ADT data respectively, suggesting that 0.1% of eddies

701   was less detected in allsat ADT than in twosat ADT. From 1 January 2000 to 13 May 2019

702   when the allsat ADT data were mainly derived from 3 or more altimeters, 117582 and 117359

703   eddies were detected from the twosat and allsat ADT data respectively, suggesting that 0.2%

704   of eddies was less detected in allsat ADT than in twosat ADT. The satellite sampling has a

705   relatively small effect on the detection of eddies in the GoM.

706   In this study, we focus on describing the characteristics of the robust mesoscale eddies in the

707   GoM, and some characteristics such as the temporal and spatial patterns of eddies still need

708   further dynamical explanations. Previous studies indicate that mesoscale eddies in the eastern

709   GoM likely arise from dynamic instabilities, such as barotropic and baroclinic instabilities

710   (e.g., Chérubin et al., 2006; Donohue et al., 2016a; Pichevin & Nof, 1997; Sturges & Leben,

711   2000; Vukovich & Maul, 1985; Yang et al., 2020; Zavala-Hidalgo et al., 2003). In the future,

712   dynamic analyses such as eddy energy may shed light on the detailed mechanisms of the

713   temporal and spatial variability of mesoscale eddies in the GoM.

714

715   **Data Availability**

716   The daily DT2018 ADT data (Taburet et al., 2019) from two altimeter satellites used for eddy

717   detection   was   provided   by   the   C3S

718   (https://cds.climate.copernicus.eu/cdsapp#!/dataset/satellite-sea-level-global?tab=form).

719   Besides, the daily DT2018 ADT data from multi-mission altimeter satellites used to examine

720   the   influence   of   satellite   sampling   on   eddy   detection   is

721   SEALEVEL_GLO_PHY_L4_REP_OBSERVATIONS_008_047 that was produced and

722   provided   by   CMEMS   (https://resources.marine.copernicus.eu/product-

723   detail/SEALEVEL_GLO_PHY_L4_MY_008_047/INFORMATION).   TOPEX/Poseidon

724   (T/P) along-track ADT data from 2 January 1996 to 3 December 1999 were used to examine

725   the effective spatial resolution of the gridded ADT product in the GoM and were provided by

726   CMEMS. Since the eddy traveling speeds were compared with the first-mode baroclinic

727   Rossby wave speeds, the atlas of the first-baroclinic Rossby radius of deformation was also

728   used and downloaded at https://ceoas.oregonstate.edu/rossby_radius (Chelton et al., 1998). The

729   multivariate ENSO index (MEI V2) (e.g., Zhang T. et al., 2019) from National Oceanic and

730   Atmospheric Administration (NOAA) Physical Sciences Laboratory, NAO index (Hurrell,

731   1995) from NOAA Climate Prediction Center, and AMM index (Chiang & Vimont, 2004) from

732   University of Wisconsin were used to examine possible relationships between the eddy activity

733   in the GoM and climate modes. The MEI, NAO index, and AMM index were downloaded at

734   https://psl.noaa.gov/data/climateindices/list/.

735

736   **Author contribution:** Yingli Zhu and Xinfeng Liang designed the experiments and Yingli
737   Zhu carried them out. Yingli Zhu prepared the manuscript with contributions from all co-
738   authors.

739

740   **Competing interests:** The authors declare that they have no conflict of interest.

741

742   **Acknowledgments**
743   The work was supported in part by the Gulf of Mexico Research Initiative through Grant G-
744   231804   and   the   National   Aeronautics   and   Space   Administration   through   Grant
745   80NSSC20K0757.

746

747   **References**

748   Alvera-Azcárate, A., Barth, A., & Weisberg, R. H.: The Surface Circulation of the Caribbean
749   Sea and the Gulf of Mexico as Inferred from Satellite Altimetry, Journal of Physical
750   Oceanography, 39(3), 640-657. https://doi.org/10.1175/2008JPO3765.1, 2009.

751   Amores, A., Jordà, G., Arsouze, T., & Le Sommer, J.: Up to what extent can we characterize
752   ocean eddies using present-day gridded altimetric products? Journal of Geophysical
753   Research: Oceans, 123, 7220– 7236. https://doi.org/10.1029/2018JC014140, 2018.

754   Beron-Vera, F. J., Olascoaga, M. J., Wang, Y., Triñanes, J., & Pérez-Brunius, P.: Enduring
755   Lagrangian coherence of a Loop Current ring assessed using independent observations.
756   *Scientific Reports*, 8(1), 11275. https://doi.org/10.1038/s41598-018-29582-5, 2018.

757   Biggs, D. C., Fargion, G. S., Hamilton, P., & Leben, R. R.: Cleavage of a gulf of mexico loop
758   current eddy by a deep water cyclone. Journal of Geophysical Research: Oceans, 101 (C9),
759   20629-20641. https://doi.org/10.1029/96JC01078, 1996.

760   Bosart, L. F., Bracken, W. E., Molinari, J., Velden, C. S., & Black, P. G.: Environmental
761   Influences on the Rapid Intensification of Hurricane Opal (1995) over the Gulf of Mexico.
762   *Monthly Weather Review*, 128(2), 322-352. https://doi.org/10.1175/1520-
763   0493(2000)128<0322:EIOTRI>2.0.CO;2, 2000.

764   Brokaw, R. J., Subrahmanyam, B., & Morey, S. L.: Loop current and eddy-driven salinity
765   variability in the Gulf of Mexico. *Geophysical Research Letters*, 46(11), 5978-5986.
766   https://doi.org/10.1029/2019GL082931, 2019.

767   Brokaw, R. J., Subrahmanyam, B., Trott, C. B., & Chaigneau, A.: Eddy surface

768   characteristics and vertical structure in the Gulf of Mexico from satellite observations and

769   model simulations. *Journal of Geophysical Research: Oceans*, 125(2), e2019JC015538.

770   https://doi.org/10.1029/2019JC015538, 2020.

771   Castelao, R. M., & He, R.: Mesoscale eddies in the South Atlantic Bight. *Journal of*

772   *Geophysical Research: Oceans*, 118(10), 5720-5731. https://doi.org/10.1002/jgrc.20415,

773   2013.

774   Chaigneau, A., Gizolme, A., & Grados, C.: Mesoscale eddies off Peru in altimeter records:

775   Identification algorithms and eddy spatio-temporal patterns. *Progress in Oceanography*,

776   79(2), 106-119. https://doi.org/10.1016/j.pocean.2008.10.013, 2008.

777   Chang, Y.-L., & Oey, L.-Y.: Eddy and Wind-Forced Heat Transports in the Gulf of Mexico.

778   *Journal of Physical Oceanography*, 40(12), 2728-2742.

779   https://doi.org/10.1175/2010JPO4474.1, 2010.

780   Chang, Y.-L., & Oey, L.-Y.: Why does the loop current tend to shed more eddies in summer

781   and winter? *Geophysical Research Letters*, 39(5). https://doi.org/10.1029/2011GL050773,

782   2012.

783   Chang, Y.-L., & Oey, L.-Y.: Loop Current Growth and Eddy Shedding Using Models and

784   Observations: Numerical Process Experiments and Satellite Altimetry Data. *Journal of*

785   *Physical Oceanography*, 43(3), 669-689. https://doi.org/10.1175/JPO-D-12-0139.1, 2013.

786   Chelton, D. B., deSzoeke, R. A., Schlax, M. G., El Naggar, K., & Siwertz, N.: Geographical

787   Variability of the First Baroclinic Rossby Radius of Deformation. *Journal of Physical*

788   *Oceanography*, 28(3), 433-460. https://doi.org/10.1175/1520-

789   0485(1998)028<0433:GVOTFB>2.0.CO;2, 1998.

790   Chelton, D. B., Schlax, M. G., & Samelson, R. M.: Global observations of nonlinear

791   mesoscale eddies. *Progress in Oceanography*, 91(2), 167 - 216.

792   https://doi.org/10.1016/j.pocean.2011.01.002, 2011.

793   Chelton, D. B., Schlax, M. G., Samelson, R. M., & de Szoeke, R. A.: Global observations of

794   large oceanic eddies. *Geophysical Research Letters*, 34(15).

795   https://doi.org/10.1029/2007GL030812, 2007.

796   Chen, G., Hou Y., and Chu X.: Mesoscale eddies in the South China Sea: Mean properties,

797   spatiotemporal variability, and impact on thermohaline structure, *J. Geophys. Res.*, 116,

798   C06018. https://doi.org/doi:10.1029/2010JC006716, 2011.

799   Chérubin, L. M., Morel, Y., & Chassignet, E. P.: Loop current ring shedding: The formation

800   of cyclones and the effect of topography. *Journal of Physical Oceanography*, 36(4), 569-591.

801   https://doi.org/10.1175/JPO2871.1, 2006.

802   Chiang, J. C. H., & Vimont, D. J.: Analogous Pacific and Atlantic Meridional Modes of

803   Tropical Atmosphere–Ocean Variability, *Journal of Climate*, *17*(21), 4143-4158.

804   https://doi.org/10.1175/JCLI4953.1, 2004.

805   Donohue, K., Watts, D., Hamilton, P., Leben, R., & Kennelly, M.: Loop current eddy

806   formation and baroclinic instability. *Dyn. Atmos. Oceans*, 76, 195-216. (The Loop Current

807   Dynamics Experiment). https://doi.org/10.1016/j.dynatmoce.2016.01.004, 2016a.

808   Donohue, K. A., Watts, D. R., Hamilton, P., Leben, R., Kennelly, M., & Lugo-Fernández, A.:

809   Gulf of Mexico Loop Current path variability. *Dyn. Atmos. Oceans*, 76, 174-194.

810   http://dx.doi.org/10.1016/j.dynatmoce.2015.12.003, 2016b.

811   Dukhovskoy, D. S., Leben, R. R., Chassignet, E. P., Hall, C. A., Morey, S. L., Nedbor-Gross,

812   R.: Characterization of the uncertainty of loop current metrics using a multidecadal numerical

813   simulation and altimeter observations. *Deep Sea Research Part I: Oceanographic Research*

814   *Papers*, 100, 140-158. https://doi.org/10.1016/j.dsr.2015.01.005, 2015.

815   Elliott, B. A.: Anticyclonic rings in the Gulf of Mexico. *Journal of Physical Oceanography*,

816   12(11), 1292-1309. https://doi.org/10.1175/1520-0485(1982)012<1292:ARITGO>2.0.CO;2,

817   1982.

818   Faghmous, J. H., Frenger, I., Yao, Y., Warmka, R., Lindell, A., & Kumar, V.: A daily global

819   mesoscale ocean eddy dataset from satellite altimetry. *Scientific Data*, 2, 150028.

820   https://doi.org/10.1038/sdata.2015.28, 2015.

821   Flierl R. G.: Particle motions in large-amplitude wave fields, *Geophysical & Astrophysical*

822   *Fluid Dynamics*, 18:1-2, 39-74, https://doi.org/10.1080/03091928108208773, 1981.

823   Fratantoni, P. S., Lee, T. N., Podesta, G. P., & Muller-Karger, F.: The influence of loop

824   current perturbations on the formation and evolution of tortugas eddies in the southern straits

825   of florida. *Journal of Geophysical Research: Oceans*, 103 (C11), 24759-24779.

826   https://doi.org/10.1029/98JC02147, 1998.

827   Frolov, S. A., Sutyrin, G. G., Rowe, G. D., & Rothstein, L. M.: Loop current eddy interaction

828   with the western boundary in the gulf of mexico. *Journal of Physical Oceanography*, 34 (10),

829   2223-2237. https://doi.org/10.1175/1520-0485(2004)034<2223:LCEIWT>2.0.CO;2, 2004.

830 Hall, C. A., & Leben, R. R.: Observational evidence of seasonality in the timing of loop

831 current eddy separation. *Dynamics of Atmospheres and Oceans*, 76, 240 - 267. (The Loop

832 Current Dynamics Experiment). https://doi.org/10.1016/j.dynatmoce.2016.06.002, 2016.

833 Halo, I., Backeberg, B., Penven, P., Ansorge, I., Reason, C., & Ullgren, J.: Eddy properties in

834 the Mozambique Channel: A comparison between observations and two numerical ocean

835 circulation models. *Deep Sea Research Part II: Topical Studies in Oceanography*, 100, 38-

836 53. https://doi.org/10.1016/j.dsr2.2013.10.015, 2014.

837 Hamilton, P.: Lower continental slope cyclonic eddies in the central Gulf of Mexico. *Journal*

838 *of Geophysical Research: Oceans*, 97(C2), 2185-2200. https://doi.org/10.1029/91JC01496,

839 1992.

840 Hamilton, P.: Eddy statistics from lagrangian drifters and hydrography for the northern gulf

841 of mexico slope. *Journal of Geophysical Research: Oceans*, 112 (C9).

842 https://doi.org/10.1029/2006JC003988, 2007.

843 Hamilton, P., Berger, T. J., & Johnson, W.: On the structure and motions of cyclones in the

844 northern gulf of mexico. *Journal of Geophysical Research: Oceans*, 107 (C12), 1-1-1-18.

845 https://doi.org/10.1029/1999JC000270, 2002.

846 Hamilton, P., Donohue, K., Hall, C., Leben, R. R., Quian, H., Sheinbaum, J., & Watts, D. R.:

847 Observations and dynamics of the loop current (Tech. Rep. No. OCS Study BOEM 2015-

848 006). New Orleans, LA: U.S. Dept. of the Interior, Bureau of Ocean Energy Management,

849 Gulf of Mexico OCS Region, 2014.

850 Hamilton, P., Fargion, G. S., & Biggs, D. C.: Loop Current Eddy Paths in the Western Gulf

851 of Mexico. *Journal of Physical Oceanography*, 29(6), 1180- 1207.

852 https://doi.org/10.1175/1520-0485(1999)029<1180:LCEPIT>2.0.CO;2, 1999.

853 Hamilton, P., Lugo-Fernández, A., & Sheinbaum, J.: A Loop Current experiment: Field and

854 remote measurements. *Dyn. Atmos. Oceans*, 76, 156-173.

855 https://doi.org/10.1016/j.dynatmoce.2016.01.005, 2016.

856 Hong, X., Chang, S. W., Raman, S., Shay, L. K., & Hodur, R.: The Interaction between

857 Hurricane Opal (1995) and a Warm Core Ring in the Gulf of Mexico. *Monthly Weather*

858 *Review*, 128(5), 1347-1365. https://doi.org/10.1175/1520-

859 0493(2000)128<1347:TIBHOA>2.0.CO;2, 2000.

860 Huang, M., Liang, X., Zhu, Y., Liu, Y., & Weisberg, R. H.: Eddies connect the tropical

861 Atlantic Ocean and the Gulf of Mexico. *Geophysical Research Letters*, 48,

862 e2020GL091277. https://doi.org/10.1029/2020GL091277, 2021.

863   Huang, H., Walker, N. D., Hsueh, Y., Chao, Y., & Leben, R. R.: An Analysis of Loop

864   Current Frontal Eddies in a 1/6° Atlantic Ocean Model Simulation. *Journal of Physical*

865   *Oceanography*, 43(9), 1924-1939. https://doi.org/10.1175/JPO-D-12-0227.1, 2013.

866   Hurlburt, H. E., & Thompson, J. D.: A Numerical Study of Loop Current Intrusions and Eddy

867   Shedding. *Journal of Physical Oceanography*, 10 (10), 1611- 1651.

868   https://doi.org/10.1175/1520-0485(1980)010<1611:ANSOLC>2.0.CO;2, 1980.

869   Hurrell, J.W.: Decadal trends in the North Atlantic Oscillation and relationships to regional

870   temperature and precipitation. *Science*, 269, 676-679.

871   https://doi.org/10.1126/science.269.5224.676, 1995.

872   Jouanno, J., Ochoa, J., Pallàs-Sanz, E., Sheinbaum, J., Andrade-Canto, F., Candela, J., &

873   Molines, J.-M.: Loop Current Frontal Eddies: Formation along the Campeche Bank and

874   Impact of Coastally Trapped Waves. *Journal of Physical Oceanography*, 46(11), 3339-3363.

875   https://doi.org/10.1175/JPO-D-16-0052.1, 2016.

876   Kang, D., & Curchitser, E. N.: Gulf stream eddy characteristics in a high resolution ocean

877   model. *Journal of Geophysical Research: Oceans*, 118(9), 4474-4487.

878   https://doi.org/10.1002/jgrc.20318, 2013.

879   Kirwan A. D., Lewis, J. K., Indest, A. W., Reinersman, P., & Quintero, I.: Observed and

880   simulated kinematic properties of loop current rings. *Journal of Geophysical Research:*

881   *Oceans*, 93(C2), 1189-1198. https://doi.org/10.1029/JC093iC02p01189, 1988.

882   Kirwan A. D., Merrell Jr., W. J., Lewis, J. K., & Whitaker, R. E.: Lagrangian observations of

883   an anticyclonic ring in the western gulf of mexico. *Journal of Geophysical Research:*

884   *Oceans*, 89(C3), 3417-3424. https://doi.org/10.1029/JC089iC03p03417, 1984.

885   Kurian, J., Colas, F., Capet, X., McWilliams, J. C., & Chelton, D. B.: Eddy properties in the

886   California Current System. *Journal of Geophysical Research: Oceans*, 116(C8).

887   https://doi.org/10.1029/2010JC006895, 2011.

888   Laxenaire, R., Speich, S., Blanke, B., Chaigneau, A., Pegliasco, C., & Stegner, A.:

889   Anticyclonic eddies connecting the western boundaries of Indian and Atlantic Oceans.

890   *Journal of Geophysical Research: Oceans*, 123, 7651–7677.

891   https://doi.org/10.1029/2018JC014270, 2018.

892   Leben, R. R.: Altimeter-derived loop current metrics, *Circulation in the Gulf of Mexico:*

893   *Observations and models* (pp. 181–201). Washington, DC: American Geophysical Union

894   (AGU). https://doi.org/10.1029/161GM15, 2005.

895   Leben, R. R., & Born, G. H.: Tracking loop current eddies with satellite altimetry. *Advances*

896   *in Space Research*, 13(11), 325-333. https://doi.org/10.1016/0273-1177(93)90235-4, 1993.

897   Le Hénaff, M., Kourafalou, V. H., Dussurget, R., & Lumpkin, R.: Cyclonic activity in the

898   eastern Gulf of Mexico: Characterization from along-track altimetry and in situ drifter

899   trajectories. *Progress in Oceanography*, 120, 120-138.

900   https://doi.org/10.1016/j.pocean.2013.08.002, 2014.

901   Le Hénaff, M., Kourafalou, V. H., Morel, Y., & Srinivasan, A.: Simulating the dynamics and

902   intensification of cyclonic Loop Current Frontal Eddies in the Gulf of Mexico. *Journal of*

903   *Geophysical Research: Oceans*, 117(C2). https://doi.org/10.1029/2011JC007279, 2012.

904   Le Traon, P. Y., & Dibarboure, G.: Mesoscale Mapping Capabilities of Multiple-Satellite

905   Altimeter Missions. *Journal of Atmospheric and Oceanic Technology*, 16(9), 1208-1223.

906   https://doi.org/10.1175/1520-0426(1999)016<1208:MMCOMS>2.0.CO;2, 1999.

907   Le Vu, B., Stegner, A., & Arsouze, T.: Angular Momentum Eddy Detection and Tracking

908   Algorithm (AMEDA) and Its Application to Coastal Eddy Formation. *Journal of*

909   *Atmospheric and Oceanic Technology*, 35(4), 739-762. https://doi.org/10.1175/JTECH-D-17-

910   0010.1, 2018.

911   Lewis, J. K., Kirwan Jr., A. D., & Forristall, G. Z.: Evolution of a warm-core ring in the Gulf

912   of Mexico: Lagrangian observations. *Journal of Geophysical Research: Oceans*, 94(C6),

913   8163-8178. https://doi.org/10.1029/JC094iC06p08163, 1989.

914   Lian, Z., Sun, B., Wei, Z., Wang, Y., & Wang, X.: Comparison of Eight Detection

915   Algorithms for the Quantification and Characterization of Mesoscale Eddies in the South

916   China Sea. *Journal of Atmospheric and Oceanic Technology*, 36(7), 1361-1380.

917   https://doi.org/10.1175/JTECH-D-18-0201.1, 2019.

918   Lindo-Atichati, D., Bringas, F., & Goni, G.: Loop current excursions and ring detachments

919   during 1993-2009. *International Journal of Remote Sensing*, 34(14), 5042-5053.

920   https://doi.org/10.1080/01431161.2013.787504, 2013.

921   Maslo, A., Azevedo Correia de Souza, J. M., & Pardo, J. S.: Energetics of the Deep Gulf of

922   Mexico. *Journal of Physical Oceanography*, 50 (6), 1655-1675. https://doi.org/10.1175/JPO-

923   D-19-0308.1, 2020

924   Mason, E., Ruiz, S., Bourdalle-Badie, R., Reffray, G., García-Sotillo, M., and Pascual, A.:

925   New insight into 3-D mesoscale eddy properties from CMEMS operational models in the

926   western Mediterranean, *Ocean Science.*, 15, 1111–1131. https://doi.org/10.5194/os-15-1111-

927   2019, 2019.

928   Meunier, T., Pallás-Sanz, E., Tenreiro, M., Portela, E., Ochoa, J., Ruiz-Angulo, A., & Cusí,

929   S.: The vertical structure of a loop current eddy. *Journal of Geophysical Research: Oceans*,

930   123(9), 6070-6090. https://doi.org/10.1029/2018JC013801, 2018.

931   Murphy, S. J., Hurlburt, H. E., & O'Brien, J. J.: The connectivity of eddy variability in the

932   Caribbean Sea, the Gulf of Mexico, and the Atlantic Ocean. *Journal of Geophysical*

933   *Research: Oceans*, 104(C1), 1431-1453. https://doi.org/10.1029/1998JC900010, 1999.

934   Oey, L.-Y., Lee, H.-C., & Schmitz Jr., W. J.: Effects of winds and Caribbean eddies on the

935   frequency of loop current eddy shedding: A numerical model study. *Journal of Geophysical*

936   *Research: Oceans*, 108(C10). https://doi.org/10.1029/2002JC001698, 2003.

937   Okubo, A.: Horizontal dispersion of floatable particles in the vicinity of velocity singularities

938   such as convergences. *Deep Sea Research*, 17(3), 445 - 454. https://doi.org/10.1016/0011-

939   7471(70)90059-8, 1970.

940   Paluszkiewicz, T., Atkinson, L. P., Posmentier, E. S., & McClain, C. R.: Observations of a

941   loop current frontal eddy intrusion onto the West Florida Shelf. *Journal of Geophysical*

942   *Research: Oceans*, 88(C14), 9639-9651. https://doi.org/10.1029/JC088iC14p09639, 1983.

943   Philander S. G.: El Niño, La Niña, and the Southern Oscillation (Academic, London), 1990.

944   Pegliasco, C., Chaigneau, A., Morrow, R., Dumas, F.: Detection and tracking of mesoscale

945   eddies in the Mediterranean Sea: A comparison between the Sea Level Anomaly and the

946   Absolute Dynamic Topography fields. *Advances in Space Research*, 68(2), 401-419.

947   https://doi.org/10.1016/j.asr.2020.03.039, 2021.

948   Pichevin, T., & Nof, D.: The momentum imbalance paradox. *Tellus A: Dynamic Meteorology*

949   *and Oceanography*, 49(2), 298-319. https://doi.org/10.3402/tellusa.v49i2.14484, 1997.

950   Pujol, M.-I., Faugère, Y., Taburet, G., Dupuy, S., Pelloquin, C., Ablain, M., & Picot, N.:

951   DUACS DT2014: the new multi-mission altimeter data set reprocessed over 20 years. *Ocean*

952   *Science*, 12(5), 1067–1090. https://doi.org/10.5194/os-12-1067-2016, 2016.

953   Rivas, D., Badan, A., Sheinbaum, J., Ochoa, J., & Candela, J.: Vertical Velocity and Vertical

954   Heat Flux Observed within Loop Current Eddies in the Central Gulf of Mexico. *Journal of*

955   *Physical Oceanography*, 38(11), 2461-2481. https://doi.org/10.1175/2008JPO3755.1, 2008.

956   Rodriguez-Vera, G., R. Romero-Centeno, C. L. Castro, and V. M. Castro: Coupled

957   Interannual Variability of Wind and Sea Surface Temperature in the Caribbean Sea and the

958   Gulf of Mexico. *J. Climate*, **32**, 4263–4280, https://doi.org/10.1175/JCLI-D-18-0573.1, 2019.

959   Rudnick, D. L., Gopalakrishnan, G., & Cornuelle, B. D.: Cyclonic Eddies in the Gulf of

960   Mexico: Observations by Underwater Gliders and Simulations by Numerical Model. *Journal*

961   *of Physical Oceanography*, 45(1), 313-326. https://doi.org/10.1175/JPO-D-14-0138.1, 2015.

962   Saraceno, M., Strub, P. T., & Kosro, P. M.: Estimates of sea surface height and near-surface

963   alongshore coastal currents from combinations of altimeters and tide gauges. *Journal of*

964   *Geophysical Research: Oceans*, 113(C11). https://doi.org/10.1029/2008JC004756, 2008.

965   Smith, I., David C.: A Numerical Study of Loop Current Eddy Interaction with Topography

966   in the Western Gulf of Mexico. *Journal of Physical Oceanography*, 16 (7), 1260-1272.

967   https://doi.org/10.1175/1520-0485(1986)016<1260:ANSOLC>2.0.CO;2, 1986.

968   Sturges, W., & Leben, R.: Frequency of ring separations from the loop current in the Gulf of

969   Mexico: A revised estimate. *Journal of Physical Oceanography*, 30(7), 1814-1819.

970   https://doi.org/10.1175/1520-0485(2000)030<1814:FORSFT>2.0.CO;2, 2000.

971   Taburet, G., Sanchez-Roman, A., Ballarotta, M., Pujol, M.-I., Legeais, J.-F., Fournier, F.,

972   Faugere, Y., & Dibarboure, G.: DUACS DT2018: 25 years of reprocessed sea level altimetry

973   products, Ocean Sci., 15, 1207–1224, https://doi.org/10.5194/os-15-1207-2019, 2019.

974   Vidal, V. M. V., Vidal, F. V., & Pérez-Molero, J. M.: Collision of a loop current anticyclonic

975   ring against the continental shelf slope of the western Gulf of Mexico. *Journal of*

976   *Geophysical Research: Oceans*, 97(C2), 2155-2172. https://doi.org/10.1029/91JC00486,

977   1992.

978   Vukovich, F. M.: Climatology of ocean features in the Gulf of Mexico using satellite remote

979   sensing data. *Journal of Physical Oceanography*, 37(3), 689-707.

980   https://doi.org/10.1175/JPO2989.1, 2007.

981   Vukovich, F. M.: Changes in the loop current's eddy shedding in the period 2001-2010.

982   International *Journal of Oceanography*, 2012, 18. https://doi.org/10.1155/2012/439042,

983   2012.

984   Vukovich, F. M., & Crissman, B. W.: Aspects of warm rings in the Gulf of Mexico. *Journal*

985   *of Geophysical Research: Oceans*, 91(C2), 2645-2660.

986   https://doi.org/10.1029/JC091iC02p02645, 1986.

987   Vukovich, F. M., & Maul, G. A.: Cyclonic Eddies in the Eastern Gulf of Mexico. *Journal of*

988   *Physical Oceanography*, 15(1), 105-117. https://doi.org/10.1175/1520-

989   0485(1985)015<0105:CEITEG>2.0.CO;2, 1985.

990   Wallace, J. M., & Gutzler, D. S.: Teleconnections in the Geopotential Height Field during the

991   Northern Hemisphere Winter, *Monthly Weather Review*, *109*(4), 784-812.

992   https://doi.org/10.1175/1520-0493(1981)109<0784:TITGHF>2.0.CO;2, 1981.

993   Walker, N., Leben, R., Anderson, S., Feeney, J., Coholan, P., & Sharma, N.: Loop current

994   frontal eddies based on satellite remote sensing and drifter data (Tech. Rep. No. OCS Study

995   MMS 2009-023). New Orleans, LA: U.S. Dept. of the Interior, Minerals Management

996   Service, Gulf of Mexico OCS Region, 2009.

997   Weiss, J.: The dynamics of enstrophy transfer in two-dimensional hydrodynamics. *Physica*

998   *D: Nonlinear Phenomena*, 48(2), 273-294. https://doi.org/10.1016/0167-2789(91)90088-Q,

999   1991

1000   Yang, Y., Weisberg, R. H., Liu, Y., & San Liang, X.: Instabilities and Multiscale Interactions

1001   Underlying the Loop Current Eddy Shedding in the Gulf of Mexico. *Journal of Physical*

1002   *Oceanography*, 50(5), 1289-1317. https://doi.org/10.1175/JPO-D-19-0202.1, 2020.

1003   Zavala-Hidalgo, J., Morey, S. L., & O'Brien, J. J.: Cyclonic Eddies Northeast of the

1004   Campeche Bank from Altimetry Data. *Journal of Physical Oceanography*, 33(3), 623-629.

1005   https://doi.org/10.1175/1520-0485(2003)033<0623:CENOTC>2.0.CO;2, 2003.

1006   Zhang, T, A. Hoell, J. Perlwitz, J. Eischeid, D. Murray, M. Hoerling and T. Hamill: Towards

1007   Probabilistic Multivariate ENSO Monitoring, *Geophys. Res. Lett.*, 46,

1008   https://doi.org/10.1029/2019GL083946, 2019.

1009   Zhang, Y., Hu, C., Liu, Y., Weisberg, R. H., & Kourafalou, V. H.: Submesoscale and

1010   mesoscale eddies in the florida straits: Observations from satellite ocean color measurements.

1011   *Geophysical Research Letters*, 46(22), 13262-13270. https://doi.org/10.1029/2019GL083999,

1012   2019.

1013   Zhu, Y., & Liang, X.: Coupling of the surface and near-bottom currents in the Gulf of

1014   Mexico. *Journal of Geophysical Research:*

1015   *Oceans*, 125, e2020JC016488. https://doi.org/10.1029/2020JC016488, 2020.

1016

1017